

## HST EMISSION-LINE IMAGES OF NEARBY 3CR RADIO GALAXIES: TWO PHOTOIONIZATION, ACCRETION AND FEEDBACK MODES

RANIERI D. BALDI<sup>1,2</sup>, JAVIER RODRÍGUEZ ZAURÍN<sup>2,3</sup>, MARCO CHIABERGE<sup>2,4</sup>,  
ALESSANDRO CAPETTI<sup>5</sup>, WILLIAM B. SPARKS<sup>2</sup>, IAN M. MCHARDY<sup>1</sup>

*Draft version November 14, 2018*

### ABSTRACT

We present *HST*/ACS narrow-band images of a low-*z* sample of 19 3C radio galaxies to study the H $\alpha$  and [O III] emissions from the narrow-line region (NLR). Based on nuclear emission line ratios, we divide the sample into High and Low Excitation Galaxies (HEGs and LEGs). We observe different line morphologies, extended line emission on kpc scale, large [O III]/H $\alpha$  scatter across the galaxies, and a radio-line alignment. In general, HEGs show more prominent emission line properties than LEGs: larger, more disturbed, more luminous, and more massive regions of ionized gas with slightly larger covering factors. We find evidence of correlations between line luminosities and (radio and X-ray) nuclear luminosities. All these results point to a main common origin, the active nucleus, which ionize the surrounding gas. However, the contribution of additional photoionization mechanism (jet shocks and star formation) are needed to account for the different line properties of the two classes.

A relationship between the accretion, photoionization and feedback modes emerges from this study. For LEGs (hot-gas accretors), the synchrotron emission from the jet represents the main source of ionizing photons. The lack of cold gas and star formation in their hosts accounts for the moderate ionized-gas masses and sizes. For HEGs (cold-gas accretors), an ionizing continuum from a standard disk and shocks from the powerful jets are the main sources of photoionization, with the contribution from star formation. These components, combined with the large reservoir of cold/dust gas brought from a recent merger, account for the properties of their extended emission-line regions.

*Subject headings:* Galaxies: active – galaxies: elliptical and lenticular, cD – galaxies: jets – quasars: emission lines – galaxies: ISM

### 1. INTRODUCTION

Radio galaxies (RGs) are among the most powerful phenomena in the Universe and represent an important class of objects for two main reasons. Firstly, they are excellent laboratories to study some of the most challenging topics in astronomy: the formation and ejection of relativistic radio jets and its connection to the central black hole (BH, e.g. Blandford et al. 1990; Livio 1999), the different modes of accretion onto the BH, the origin and lifetime of the AGN, the AGN feedback, and how the interstellar medium (ISM) affects the BH activity (e.g. Holt et al. 2003; Hopkins et al. 2006; Fabian et al. 2006; Heckman & Best 2014). Secondly, RGs are almost invariably associated with the most massive early-type galaxies (ETGs) in the local universe and likely harbor the most massive BHs (Zirbel 1996; Chiaberge & Marconi 2011). Therefore, RGs can be used as probes of the formation and evolution of giant ETGs through cosmic time in relation to their BH activity.

Leaving aside the abundant population of compact radio sources (FR 0s, Baldi et al. 2015, 2018), extended RGs can be classified as FR I or FR II (Fanaroff & Riley

1974), based on their radio morphology. FR Is show bright cores and jets, with the surface brightness decreasing away from the nuclear region, while FR IIs with their bright lobes and hot spots show the opposite trend. Interestingly, FR Is are usually located in the center of massive galaxy clusters (e.g. Owen 1996) while FR IIs are generally located in lower density environments (Hill & Lilly 1991; Zirbel 1997).

Another classification of RGs is based on the optical emission line ratios from the nuclear spectrum: high-excitation galaxies and low-excitation galaxies (HEGs and LEGs) (e.g. Hine & Longair 1979; Laing et al. 1994; Buttiglione et al. 2010). HEGs have typically FR II radio morphology, while LEGs encompass the two FR classes. The difference between HEGs and LEGs are thought to be related to a different mode of accretion. On one hand, HEGs, which are commonly interpreted as quasar-like AGN, have strong radiation field since they are powered by a standard accretion disk (Hardcastle et al. 2009). Optical and infrared studies indicate that HEGs show a large amount of cold gas (Baldi & Capetti 2008; Dicken et al. 2009; Tadhunter et al. 2014; Westhues et al. 2016), which channels towards the center and fuels the BH, establishing a cold accretion mode (Hardcastle et al. 2007; McNamara & Nulsen 2012; Best & Heckman 2012; Heckman & Best 2014). On the other hand, LEGs are fuelled by the hot phase of ISM and show evidence for the presence of a radiatively inefficient accretion disk (Balmaverde et al. 2008; Hardcastle et al. 2007). Their nuclei are synchrotron-dominated since the jet is the main ionizing source (Chiaberge et al.

Electronic address: r.baldi@soton.ac.uk

<sup>1</sup> School of Physics and Astronomy, University of Southampton, Southampton, SO17 1BJ, UK

<sup>2</sup> Space Telescope Science Institute, 3700 San Martin Drive, Baltimore, Baltimore, MD 21218.

<sup>3</sup> Department of Physics and Astronomy, University of Sheffield, Sheffield S3 7RH, UK

<sup>4</sup> Johns Hopkins University-Center for Astrophysical Sciences, 3400 N. Charles Street, Baltimore, MD 21218, USA

<sup>5</sup> INAF-Osservatorio Astrofisico di Torino, Strada Osservatorio 20, I-10025, Pino Torinese, Italy

1999; Hardcastle & Worrall 2000; Baldi et al. 2010; Hardcastle et al. 2009).

Ionizing radiation from accreting supermassive BH at the center of galaxies is believed to illuminate the narrow line region (NLR) in the host galaxies of AGN, creating emission-line regions which can extend up to kiloparsec scales (e.g. Bennert et al. 2002; Congiu et al. 2017; Sun et al. 2018).

Although the efficiency of the AGN feedback is still matter of discussion in local galaxies (see Shanguan et al. 2018), there are growing observational evidence of the AGN feedback on the ISM in radio AGN (e.g. Tremblay et al. 2009; Fabian 2012; Couto et al. 2013; Harrison et al. 2015; Roche et al. 2016; Couto et al. 2017; Harrison et al. 2018). In the so-called *quasar-mode feedback* scenario (e.g. Silk & Rees 1998; Fabian 1999), the central engine efficiently ionizes the innermost and an intermediate region of the NLR (within some kpc scale, e.g. Gómez-Guijarro et al. 2017) which show a density and ionization stratification (Balmaverde et al. 2016; Adhikari et al. 2016). Furthermore, with a radial decrease of efficiency, its radiation field can ionize the medium at larger distance from the nucleus up to some kpc (e.g. Robinson et al. 1987; Baum & Heckman 1989b). Such extended emission has a rich spectrum which is often characterized by large  $[\text{O III}]\lambda 5007/\text{H}\beta$  and  $\text{HII}\lambda 4686/\text{H}\beta$  ratios and, in some cases, includes very high ionization species such as  $[\text{Ca V}]$ ,  $[\text{Fe VIII}]$  or  $[\text{Fe X}]$  (e.g. Fosbury et al. 1982; Tadhunter et al. 1987; Erkens et al. 1997). The observed line ratios are usually explained in terms of photoionization by a central source on clouds formed by a combination of optically thin and optically thick materials (Binette et al. 1996; Robinson et al. 2000). Conversely, the so-called *radio-mode feedback* (e.g. Croton et al. 2006; Bower et al. 2006) is released in a kinetic form via radio jets, which deposit energy into the ISM and ionize the gas (Capetti et al. 2005). The majority of the local RGs are currently in a radiatively inefficient accretion regime, where kinetic feedback dominates over radiative feedback (Ishibashi et al. 2014). The two feedback modes can coexist or delayed in time in RGs, regulated by the different accretion modes and duty cycles (Okamoto et al. 2008; Bîrzan et al. 2012).

Other sources, which produce high-energy photons, could have a secondary role in the photoionization of the gas in RGs: fast radiative shocks (e.g. Evans & Dopita 1985; Dopita & Sutherland 1995; Clark et al. 1998; Groves et al. 2004), hot stars, (Allen et al. 2008), and relativistic particles associated with jets (Lea & Holman 1978).

Assuming photoionization by a central source as the dominant mechanism, the emission line luminosities from the ionized gas at large scales may be used to derive the properties of the central engine, such as the shape of the photoionizing continuum and its power (Morganti et al. 1991; Tadhunter et al. 1994). For example, the well established correlations between the optical emission lines and the 178-MHz radio power (e.g. Rawlings & Saunders 1991; Tadhunter et al. 1998), suggests a direct link between the AGN continuum and the mechanism responsible of the radio-jet production. A relation between the radio and ionized gas, as stellar content and emission lines, has been addressed as the 'alignment effect', where

the optical and infrared light is aligned along radio-jet axes (e.g. McCarthy et al. 1987; Chambers et al. 1987). It has been explained as the effect of either the dust scattering of light from a hidden quasar at the nucleus or triggering of star formation by the synchrotron jet as it propagates outward from the nucleus. Overall, although emission lines provide a simple tool to study the NLR, the details of the mechanisms involved in the production of such ionized gas are yet to be fully understood.

In this context, the *Hubble Space Telescope (HST)* offers a unique opportunity to study the spatial properties of the line emitting gas with unprecedented resolution. In this paper we present narrow-band optical *HST/ACS* observations sampling the  $\text{H}\alpha + [\text{N II}]$  and  $[\text{O III}]\lambda 5007$  emission for 19 3C RGs with  $z < 0.3$ . Tremblay et al. (2009) presented the data-set and a preliminary analysis of the images. Here we have used the most up-to-date version of the *HST/ACS* reduction pipeline that allows us to improve the quality of the data-set, which is again presented and analyzed in detail. The *HST/ACS* high-resolution data-sets allow us to study the properties of the emission line region and their variation across the NLR in the perspective of the HEG-LEG scheme. In addition, we combine our images with existing optical ground-based spectroscopic data (Buttiglione et al. 2009, 2010, 2011) (hereafter B09+) and *Chandra* X-ray observations (Massaro et al. 2010, 2012; Balmaverde et al. 2012, Torresi et al. in prep) to estimate a number of physical parameters, such as the number of ionizing photons, covering factors, and mass of ionized gas, with the aim of better understanding the nature of the ionizing source and the properties of the ionized gas itself.

We organize this paper as follows. Section 2 presents a description of the sample and the corresponding observations, while the reduction process and calibration of the data are presented in Section 3. Section 4 shows the catalogue of  $\text{H}\alpha + [\text{N II}]$  and  $[\text{O III}]$  images and the corresponding flux measurements. In addition, we show  $[\text{O III}]/\text{H}\alpha + [\text{N II}]$  emission line ratio images. Section 4 presents the results of measuring the physical parameters mentioned before. In Section 5 we discuss all the previous results in light of the two AGN classes (LEGs and HEGs). Summary and potential future observations are presented in Section 6. Throughout this paper we use  $H_0 = 71 \text{ km s}^{-1}$ ,  $\Omega_M = 0.27$  and  $\Omega_\Lambda = 0.73$ .

## 2. SAMPLE SELECTION AND OBSERVATIONS

The sample selection and observations are described in detail in Tremblay et al. (2009). To summarize, we present a sample of 19 3CR radio sources from the low- $z$  ( $z < 0.3$ ) extra-galactic radio-source Revised Third Cambridge Catalogue (3CR, Bennett 1962a,b; Spinrad et al. 1985). The sample comes from the original *HST* proposal for 98 3CR sources that was awarded for observations prior to the ACS side 2 electronics failure in January 2007. Although only 19 sources were observed (Table 1), these objects represent an unbiased sample in selection due to the nature of the *HST* snapshot mode (to fill gaps in the *HST* schedule, sources are randomly picked from the target list). Moreover, the observed 19 objects span almost the whole redshift range ( $0.0075 < z < 0.224$ ) of the original sample and show a wide variety of emission line ratios, radio power or

TABLE 1  
OBSERVING LOG

Name	z	RA	DEC	Filter	Line/Cont	$\lambda_c$	$t_{exp}$
3C		(J2000.0)	(J2000.0)			( $\text{\AA}$ )	(s)
(1)	(2)	(3)	(4)	(5)	(6)	(7)	(8)
33.0	0.0597	01 08 52.8	+13 20 14	FR647M	Cont	5828	60
				FR716N	H $\alpha$	6951	400
				FR551N	[O III]	5303	500
40.0	0.0180	01 25 59.9	-01 20 33	FR647M	Cont	5599	60
				FR656N	H $\alpha$	6674	400
				FR505N	[O III]	5092	500
78.0	0.0286	03 08 26.2	+04 06 39	FR647M	Cont	5575	60
				FR656N	H $\alpha$	6746	400
				FR505N	[O III]	5147	500
93.1	0.2430	03 48 46.9	+33 53 15	FR647M	Cont	6837	60
				FR853N	H $\alpha$	8164	400
				FR601N	[O III]	6228	500
129.0	0.0208	04 49 09.1	+45 00 39	FR647M	Cont	5620	60
				FR656N	H $\alpha$	6700	400
				FR505N	[O III]	5112	500
132.0	0.2140	04 49 09.1	+45 00 39	FR647M	Cont	6674	60
				FR782N	H $\alpha$	7966	400
				FR601N	[O III]	6078	500
136.1	0.0640	04 56 43.0	+22 49 22	FR647M	Cont	5856	60
				FR716N	H $\alpha$	6983	400
				FR551N	[O III]	5328	500
180.0	0.2200	07 27 04.5	-02 04 42	FR647M	Cont	6707	60
				FR782N	H $\alpha$	8005	400
				FR601N	[O III]	6108	500
196.1	0.1980	08 15 27.8	-03 08 27	FR647M	Cont	6587	60
				FR782N	H $\alpha$	7861	400
				FR601N	[O III]	5998	500
197.1	0.1280	08 21 33.6	+47 02 37	FR647M	Cont	6217	60
				FR716N	H $\alpha$	7414	400
				FR551N	[O III]	5657	500
219.0	0.1744	09 21 08.6	+45 38 57	FR647M	Cont	6456	60
				FR782N	H $\alpha$	7704	400
				FR601N	[O III]	5879	500
227.0	0.0858	09 47 45.1	+07 25 20	FR647M	Cont	5976	60
				FR716N	H $\alpha$	7127	400
				FR551N	[O III]	5438	500
234.0	0.1849	10 01 49.5	+28 47 09	FR647M	Cont	6510	60
				FR782N	H $\alpha$	7770	400
				FR601N	[O III]	5928	500
270.0	0.0075	12 19 23.2	+05 49 31	FR647M	Cont	5546	60
				FR656N	H $\alpha$	6611	400
				FR505N	[O III]	5044	500
285.0	0.0794	13 21 17.9	+42 35 15	FR647M	Cont	5938	60
				FR716N	H $\alpha$	7081	400
				FR551N	[O III]	5403	500
314.1	0.1197	15 10 22.5	+70 45 52	FR647M	Cont	6156	60
				FR716N	H $\alpha$	7342	400
				FR551N	[O III]	5602	500
319.0	0.1920	15 24 05.6	+54 28 18	FR647M	Cont	6554	60
				FR782N	H $\alpha$	7822	400
				FR601N	[O III]	5968	500
388.0	0.0917	18 44 02.4	+45 33 30	FR647M	Cont	6007	60
				FR716N	H $\alpha$	7164	400
				FR551N	[O III]	5466	500
390.3	0.0561	18 42 09.0	+79 46 17	FR647M	Cont	5812	60
				FR716N	H $\alpha$	6931	400
				FR551N	[O III]	5288	500

NOTE. — Log of the *HST*/ACS WFC observations (Program 10882, PI: W.B. Sparks). Col (1): 3C source name. Col (2): redshift. Col (3)-(4): right ascension and declination. Col (5)-(6): ramp filters used for the continuum, H $\alpha$  and [O III] observations, respectively. Col (7) central wavelength observed corresponding to the ramp filter configuration. Col (8): total exposure time.

spectroscopic properties. With regards to their radio morphologies, the sample consists of 4 FR Is and 14 FR IIs, taking the double-lobed 3C 314.1 apart (Table 2). In terms of their optical, spectroscopic classification, 8 of the objects in our sample are classified as LEGs, 10 are HEGs, of which four have broad lines, named Broad Line Objects (BLOs). Of particular interest is 3C 314.1, a RG whose spectral classification is Extremely Low-Excitation Galaxy (ELEG, Capetti et al.

TABLE 2  
MULTI-BAND PROPERTIES

Name	FR	optical	log L <sub>178</sub>	log L <sub>core</sub>	log L <sub>X</sub>	$\Gamma$
3C	class	class	erg s <sup>-1</sup> Hz <sup>-1</sup>	erg s <sup>-1</sup> Hz <sup>-1</sup>	erg s <sup>-1</sup>	
(1)	(2)	(3)	(4)	(5)	(6)	(7)
33	II	HEG	33.65	30.27	43.74	1.70(fix)
40	I	LEG	32.29	30.66	41.06	1.77
78	I	LEG	32.51	31.25	42.30	2.20
93.1	II	HEG	34.24	—	43.25	1.75
129	I	LEG	32.65	28.92	40.09	2.32
132	II	LEG	34.26	31.40	<41.99 <sup>a</sup>	2.35
136.1	II	HEG	33.13	29.16	<42.91	1.70(fix)
180	II	HEG	34.32	—	43.84	1.70(fix)
196.1	II	LEG	34.31	31.65	—	—
197.1	II	BLO	33.55	30.30	43.62	1.30
219	II	BLO	34.53	31.54	44.14 <sup>b</sup>	1.58
227	II	BLO	33.74	30.48	43.27 <sup>c</sup>	1.5(fix)
234	II	HEG	34.47	31.88	44.05	1.5
270	I	LEG	32.75	29.50	40.70 <sup>d</sup>	0.8
285	II	HEG	33.23	29.93	43.36	2.0(fix)
314.1	double	ELEG	33.59	29.36	—	—
319	II	LEG	34.20	29.93	<42.71	1.7(fix)
388	II	LEG	33.70	31.04	41.87 <sup>a</sup>	2.28
390.3	II	BLO	33.54	31.38	44.38	1.83

NOTE. — Col (1): 3C source name. Col (2): morphological FR type. Col (3): spectroscopic class from Buttiglione et al. (2010) - LEG = low excitation galaxy, HEG = high excitation galaxy, ELEG = extremely low excitation galaxy, BLO = broad line object. Col (4): Log of the radio power at 178 MHz. Col (5): Log of the radio core power at 5 GHz. References can be found in Buttiglione et al. (2010) and Baldi et al. (2010) Col (6): Log X-ray (2-10 keV) unabsorbed nuclear luminosities from *Chandra* data from Torresi et al. (in prep). The exceptions are: Hardcastle et al. (2009) marked by <sup>a</sup>, Shi et al. (2005) marked by <sup>b</sup>, Kataoka et al. (2011) marked by <sup>c</sup>, Balmaverde et al. (2006) marked by <sup>d</sup>. Typical error on the X-ray luminosities is 0.2 dex. Col (7): X-ray photon index  $\Gamma$  (references from Col 6.).

2011) interpreted as relic RG (Capetti et al. 2013). Table 2 summarizes the radio and spectroscopic classification of the sample. This table also collects the total radio luminosities at 178 MHz, the radio core powers (at 5 GHz) and the X-ray luminosities for the sample. The uncertainties on the radio luminosities are negligible with respect to those of the X-ray luminosities, which amount to  $\sim 0.2$  dex.

Our *HST* data-set consists of images taken with the ACS Wide Field Channel (WFC). Linear ramp filters, with typical  $\lambda$  range of 4500-7500  $\text{\AA}$  were used to image the [O III] $\lambda 5007$  and the H $\alpha$ + [N II] (hereafter H $\alpha$  for simplicity) emission from the galaxies in our sample, adjusting the central wavelength according to the redshifts of the objects. The details of the observations for the 19 galaxies of our sample are presented in Table 1.

### 3. DATA REDUCTION AND CALIBRATION

The data were reduced using the standard data reduction pipeline procedures, which employ two packages: the CALACS package, that includes dark subtraction, bias subtraction and flat-field corrections and produces calibrated images, and the MULTIDRIZZLE package, which corrects for distortion and performs cosmic ray rejection.

In order to reject cosmic rays, hot pixels and other artifacts, two exposures of 250 and 200 sec were taken for the [O III] and the H $\alpha$  emission lines, respectively. In addition, with the aim of generating “pure” emission line images, the continuum emission between the two lines was sampled using 60 seconds single exposures of the medium ramp filter FR647M centered at various wavelengths (5370-7570  $\text{\AA}$ ), depending on the wave-

TABLE 3  
HST OPTICAL PROPERTIES

Name	H $\alpha$ + [N II] flux	[O III] flux	L <sub>H<math>\alpha</math>+ [N II]</sub>	L <sub>[O III]</sub>	P <sub>[N II]</sub>	P <sub>[O III]<math>\lambda</math>4959</sub>	BLR	R <sub>flux</sub>
3C	10 <sup>-14</sup> erg s <sup>-1</sup> cm <sup>-2</sup>	10 <sup>-14</sup> erg s <sup>-1</sup> cm <sup>-2</sup>	erg s <sup>-1</sup>	erg s <sup>-1</sup>	%	%	%	kpc
(1)	(2)	(3)	(4)	(5)	(6)	(7)	(8)	(9)
33.0	8.61±0.70	12.86±0.94	41.85	42.03	50	10	-	0.95
40.0	1.50±0.14	0.20±0.03	<40.02	<39.16	-	-	-	0.25
78.0	5.05±0.80	1.02±0.11	40.96	40.27	81	-	-	0.14
93.1	3.02±0.31	2.61±0.08	42.72	42.66	65	12	-	1.03
129.0	1.05±0.21	-	40.00	-	-	-	-	0.03
132.0	0.22±0.05	-	41.46	-	-	-	-	0.59
136.1	6.36±0.75	2.68±0.21	41.78	41.41	47	-	-	0.55
180.0	2.83±0.61	7.02±1.20	42.60	42.99	50	13	-	7.00
196.1	1.34±0.26	0.35±0.06	42.17	41.58	62	10	-	3.39
197.1	0.91±0.02	0.32±0.06	41.58	41.13	25	-	58	0.27
219.0	2.88±0.42	1.56±0.25	42.38	42.11	30	-	52	0.40
227.0	22.99±1.82	5.67±0.68	42.61	42.01	1	25	95	-
234.0	15.03±1.41	25.55±2.60	43.15	43.38	22	-	-	0.76
270.0	3.90±0.73	0.39±0.08	<39.68	<38.67	-	-	-	0.07
285.0	1.07±0.25	0.91±0.20	41.21	41.14	45	-	-	1.77
314.1	0.10±0.02	0.03±0.01	40.54	40.02	53	-	-	0.36
319.0	0.14±0.03	-	41.16	-	-	-	-	0.72
388.0	1.78±0.25	0.18±0.04	41.56	40.57	76	-	-	0.32
390.3	64.96±5.52	24.18±2.1	42.67	42.25	5	30	88	-

NOTE. — Col (1): 3C source name. Col (2): total H $\alpha$ + [N II] flux. Col (3): total [O III] flux. Col (4): total H $\alpha$ + [N II] luminosity. Col (5): total [O III] luminosity. Col (6): estimated [N II] $\lambda$ 6549,6583Å percentage contribution to the flux within the wavelength range of the filter. Col (7): estimated [O III] $\lambda$ 4959Å contribution to the flux within the wavelength range of the filter. Col (8): percentage of the emission that corresponds to the broad H $\alpha$  component for those sources spectroscopically classified as BLOs. Col (9): “flux weighted radius” (see text for details).

length of the target. For these images, the cosmic rays were rejected “manually” using the routines IMEDIT in IRAF and/or CLEAN within the STARLINK package FIGARO.

The background was subtracted from the images using the average value (in electrons s<sup>-1</sup>) of a region located at the outskirts of the galaxies, avoiding the central regions.

To convert into physical units the background-subtracted images, it is possible to use, a priori, the PHOTFLAM keyword. PHOTFLAM is the inverse sensitivity (erg cm<sup>-2</sup> sec<sup>-1</sup> Å<sup>-1</sup>) and represents the flux of a source with constant F $_{\lambda}$  which produces a count rate of 1 electron per second. Given that the ACS drizzled images have units of electrons s<sup>-1</sup>, flux units of erg cm<sup>-2</sup> sec<sup>-1</sup> Å<sup>-1</sup> are obtained just by multiplying the images by the PHOTFLAM value. However, while this is adequate when the flux is approximately constant through the bandpass, it is certainly not adequate when the spectrum of the source shows a significant slope or strong emission lines within the bandwidth, which is the case for most of our observations. Therefore, in order to adequately calibrate the 3C images in flux, we first examined the spatial shape of the corresponding long-slit, optical spectra available for *all* the galaxies in our sample (B09+).

The PHOTFLAM parameter was finally used for all continuum images and for those emission-line images for which the corresponding spectra show weak emission lines in the nuclear region. Conversely, for those galaxies with evidence of significant [O III] and H $\alpha$  emission, it is more convenient to use the Equivalent Monochromatic Flux (EMFLX) of the filter. This parameter is obtained using the routine BANDPAR within SYNPHOT package in IRAF, and is calculated as follows:

$$EMFLX = URESP \times \frac{\int P_{\lambda} d\lambda}{P_{\lambda cen}} \quad (1)$$

where URESP is the response of the filter (i.e. the flux that produces 1 count per second in the passband), P $_{\lambda}$

is the dimensionless passband throughput as a function of wavelength and P $_{\lambda cen}$  is a passband throughput at the central wavelength of the filter. The data calibration performed by Tremblay et al. (2009) did not include this spectral correction across the bandwidth for the sources.

The next step during the reduction process is to align the continuum images with the corresponding emission line images. We used the routines GEOMAP and GEOTRAN in IRAF to geometrically align the images in those cases for which 3 or more foreground stars (less than 10) were present in the field of view. For the remaining cases we used the routines IMSHIFT and ROTATE in IRAF to shift and rotate the images based on features observed in the galaxy and/or present in the frame. To check the accuracy of the alignment we used the routine CENTER in IRAF to calculate the centroid of the stars in the aligned images and the position of some of the mentioned features. We estimate that the alignment accuracy is usually better than 0.5 pixels.

Once the images were aligned, the continuum emission was subtracted from the emission line images in order to produce “pure” [O III] and H $\alpha$  images. Finally, we selected a 2 $\sigma$  lower cut as a threshold to distinguish galaxy from background, where  $\sigma$  was the root mean square (rms) of the flux in a region in the field of view far from galaxy emission. The 2 $\sigma$  lower cut procedure was selected based on visual inspection of contour plots onto the continuum-subtracted emission line images. All pixels with flux values below the limit threshold were set to 0. The emission line flux from the galaxy was then measured by integrating within the limiting contour level, i.e. the contour that separates galaxy from background. Figure 1 shows an example of the process for the case of 3C 33.

### 3.1. Flux calibration accuracy

To check the flux calibration accuracy we compared the flux measurements from our images with those obtained by B09+ spectra, by convolving the spectra with the spectral response of the *HST* ACS ramp filters on

## 3C33

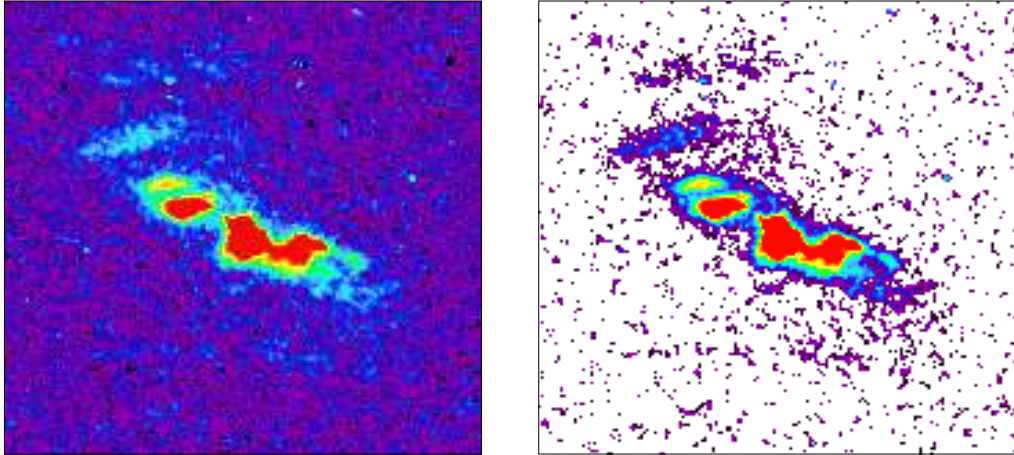


FIG. 1.— An example of the “source region” selection process for the galaxy 3C 33. On the left the raw image and on the right the final continuum-subtracted image. In the color print version, redder color corresponds to higher emission line brightness.

the same integration area. Since B09+ spectra were extracted using a  $2'' \times 2''$  box, we first analyzed the objects for which the entire emission in our images was confined in a similar area to avoid uncertainties due to the presence of extended emission. We then applied the same procedure to all galaxies in our sample, centering a  $2'' \times 2''$  box on the peak of the continuum emission in our ACS images. We found that the flux values derived using our HST images were, in general, consistent within a factor of 2 with respect to those from the long-slit spectroscopy. The exceptions are 3C 40, 3C 78 and 3C 270. In the case of 3C 78, the continuum image has a cosmic ray coinciding with the location of the nucleus. Since it is not possible to entirely correct for this effect during the reduction process, the continuum subtraction is not highly accurate for this source. For 3C 40 and 3C 270, the difference is due to fact that HST images are probably dominated by the continuum (see Sect. 4.1).

The images are not corrected for the  $[\text{N II}]\lambda\lambda 6549, 6583$  or the  $[\text{O III}]\lambda 4959$  contribution to the flux that falls within the bandpass of the ramp filters for the  $\text{H}\alpha$  and the  $[\text{O III}]\lambda 5007$ , respectively. To give an idea of such contributions we have used the B09+ optical spectra along with the STARLINK package DIPSO to model the emission line profiles with one or two Gaussians per emission line. The values are presented in Table 3. Furthermore, the spectra of BLOs show impressive broad  $\text{H}\alpha$  and  $\text{H}\beta$  components which strongly contribute to the emission of the narrow  $\text{H}\alpha$  and  $[\text{O III}]\lambda 5007$  observations, respectively. We estimated the percentage contribution of  $\text{H}\alpha$  and  $\text{H}\beta$  broad component ( $\sim 50$ -95 per cent) to correct the total emission-line luminosities for BLOs in Table 3, using the spectra from B09+.

#### 4. RESULTS

##### 4.1. The $\text{H}\alpha$ and $[\text{O III}]\lambda 5007$ images

Figure 2 (first and second columns) is a collection of the  $[\text{O III}]\lambda 5007$  and  $\text{H}\alpha$  continuum-subtracted images of all galaxies in our sample. Table 3 presents the integrated  $[\text{O III}]\lambda 5007$  and  $\text{H}\alpha$  flux values measured from those maps, which are corrected for  $\text{H}\alpha$  and  $\text{H}\beta$  broad line contribution and not for the  $[\text{O III}]\lambda 4959$  and  $[\text{N II}]\lambda 6583$  narrow

lines. In addition, the values were corrected for Galactic reddening using the Howarth (1983) extension to optical wavelengths of the Seaton (1979) reddening law, along with the  $E(B - V)$  values derived from the far-IR based maps of extinction by Schlegel et al. (1998). The mean estimated uncertainty of the fluxes is 15%, ranging between 8 and 30%.

The up-to-date version of the *HST*/ACS reduction pipeline, the correction for the spectral slope in the filter bandwidth and the correction for broad and narrow emission lines result in measured emission-line fluxes which significantly differ from the values derived by Tremblay et al. (2009) by 1–2 orders of magnitude. In addition, the line luminosities derived from our images generally agree with the values extracted from the long-slit spectra (B09+) for the sources with compact line emission. For the sources with extended line emission, our luminosities are higher than those derived from the nuclear spectra within a factor 10.

Ionized gas emission, either  $[\text{O III}]\lambda 5007$  or  $\text{H}\alpha$  is detected for the majority of objects in our sample. However, there are some cases that deserve more attention. On one hand, the optical spectra of 3C 40 and 3C 270 show weak or no evidence of ionized gas emission (B09+). Conversely, both our  $\text{H}\alpha$  and  $[\text{O III}]\lambda 5007$  images clearly reveal enhanced emission concentrated toward the nuclear region of the sources. Therefore, it is likely that their HST images are dominated by continuum and the emission lines are diluted by such a component. In this case, the emission-line fluxes, derived from the HST images, would be upper limits (Table 3). On the other hand, the HST images of 3C 129, 3C 132 and 3C 319 show no evidence for  $[\text{O III}]\lambda 5007$  emission, but a faint compact emission in the  $\text{H}\alpha$  images emerges. This evidence is consistent with their optical spectra from B09+ which show detected  $\text{H}\alpha$  and weak or non-detected  $[\text{O III}]\lambda 5007$ .

Considering the whole sample, we found that the  $\text{H}\alpha$  and  $[\text{O III}]\lambda 5007$  luminosities range from  $9.3 \times 10^{39}$  to  $1.4 \times 10^{43}$   $\text{erg s}^{-1}$  and  $4.6 \times 10^{38}$  to  $2.4 \times 10^{43}$   $\text{erg s}^{-1}$ . HEGs show larger emission-line luminosities than LEGs, on average, by a factor  $\sim 26$  and  $\sim 140$ , respectively for  $\text{H}\alpha$  and  $[\text{O III}]\lambda 5007$ .

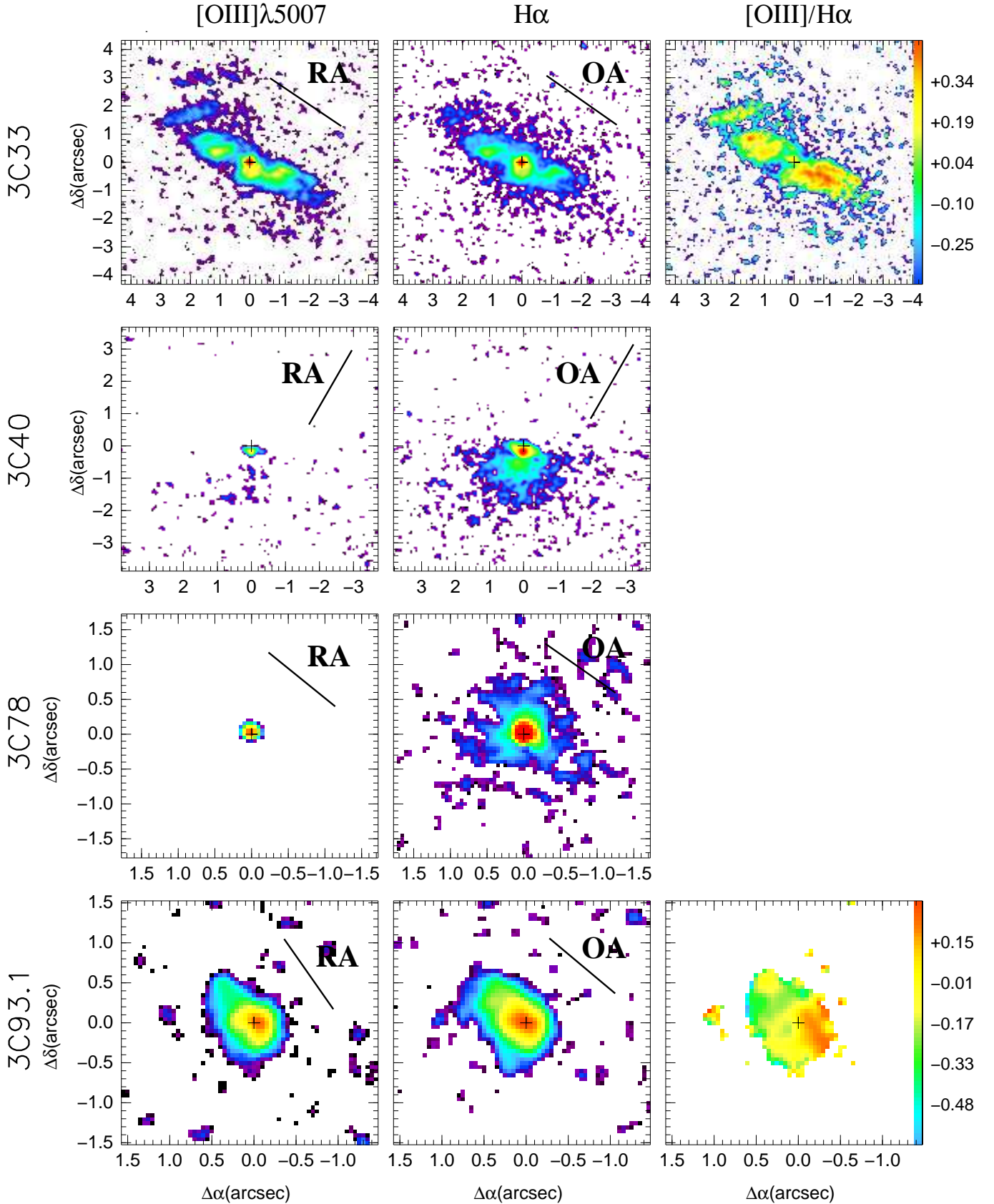


FIG. 2.— *Left and middle columns:* the  $\text{H}\alpha$  and  $[\text{O III}]\lambda 5007$  continuum-subtracted images of the sources. *Right column:* images showing the spatial distribution of the logarithm of the  $[\text{O III}]/\text{H}\alpha$  flux ratio, for those galaxies with extended emission and/or sufficient S/N to generate reliable line ratio images. The plus sign indicates the center of the galaxy defined as the maximum of the continuum emission in the corresponding continuum observation. The black-solid lines in the  $[\text{O III}]\lambda 5007$  and  $\text{H}\alpha$  images indicate the orientation of the radio (RA) and optical axis (OA) respectively (see text for details). For those objects with no clear radio and/or optical axis no lines are shown in the Figure. All images are represented in logarithmic scale. For all images North is top, East is left.



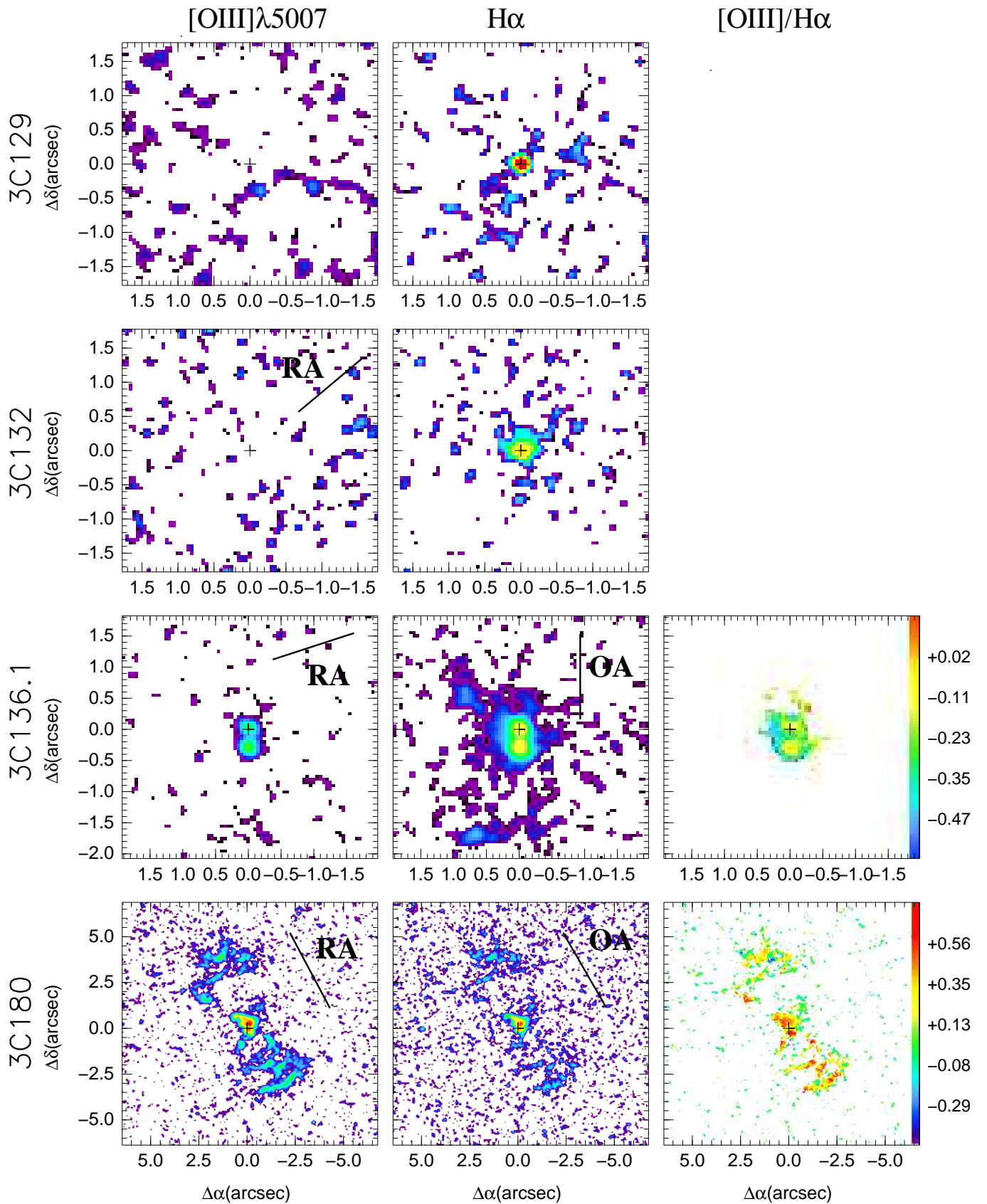


FIG. 2.— Continued

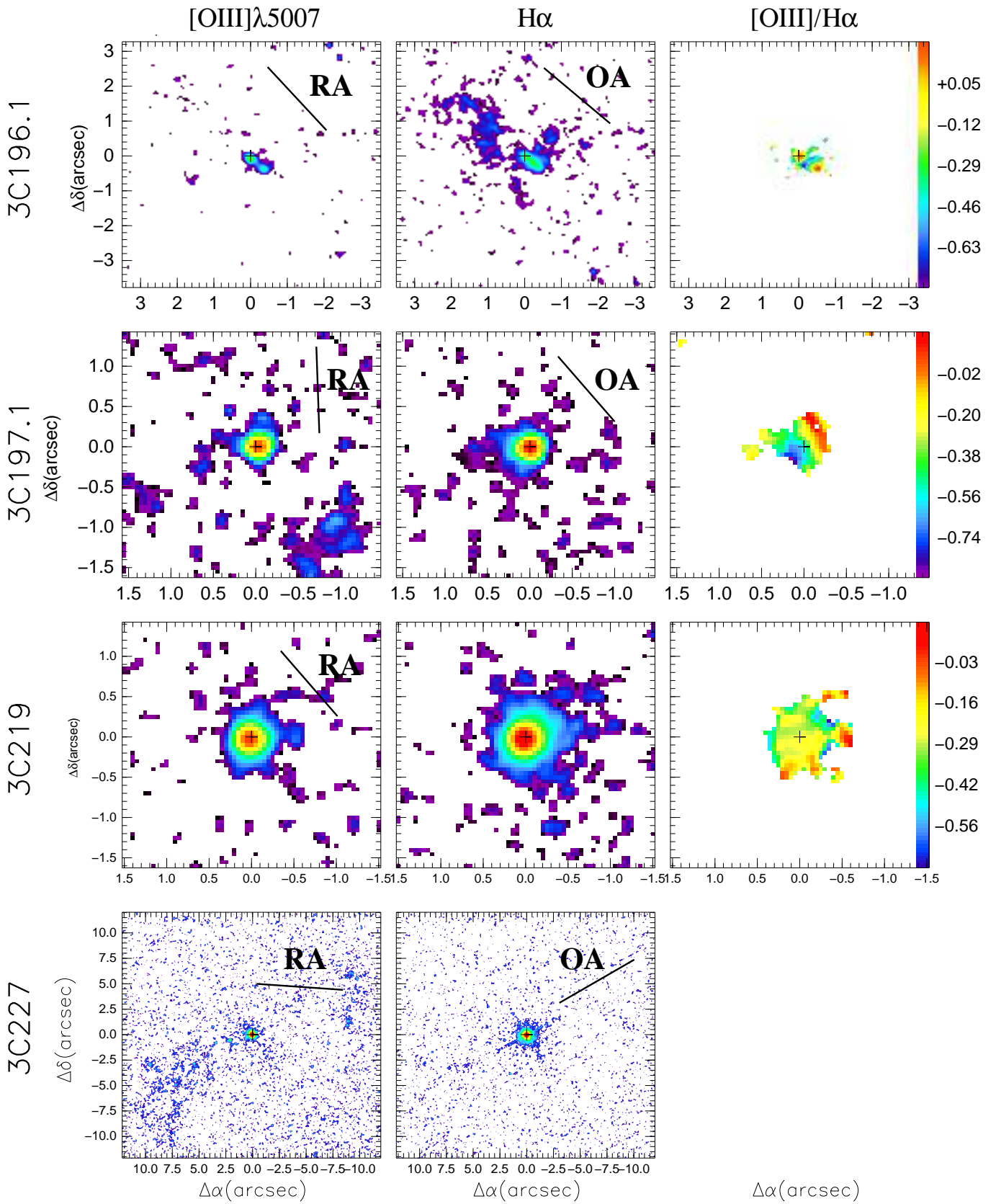


FIG. 2.— Continued



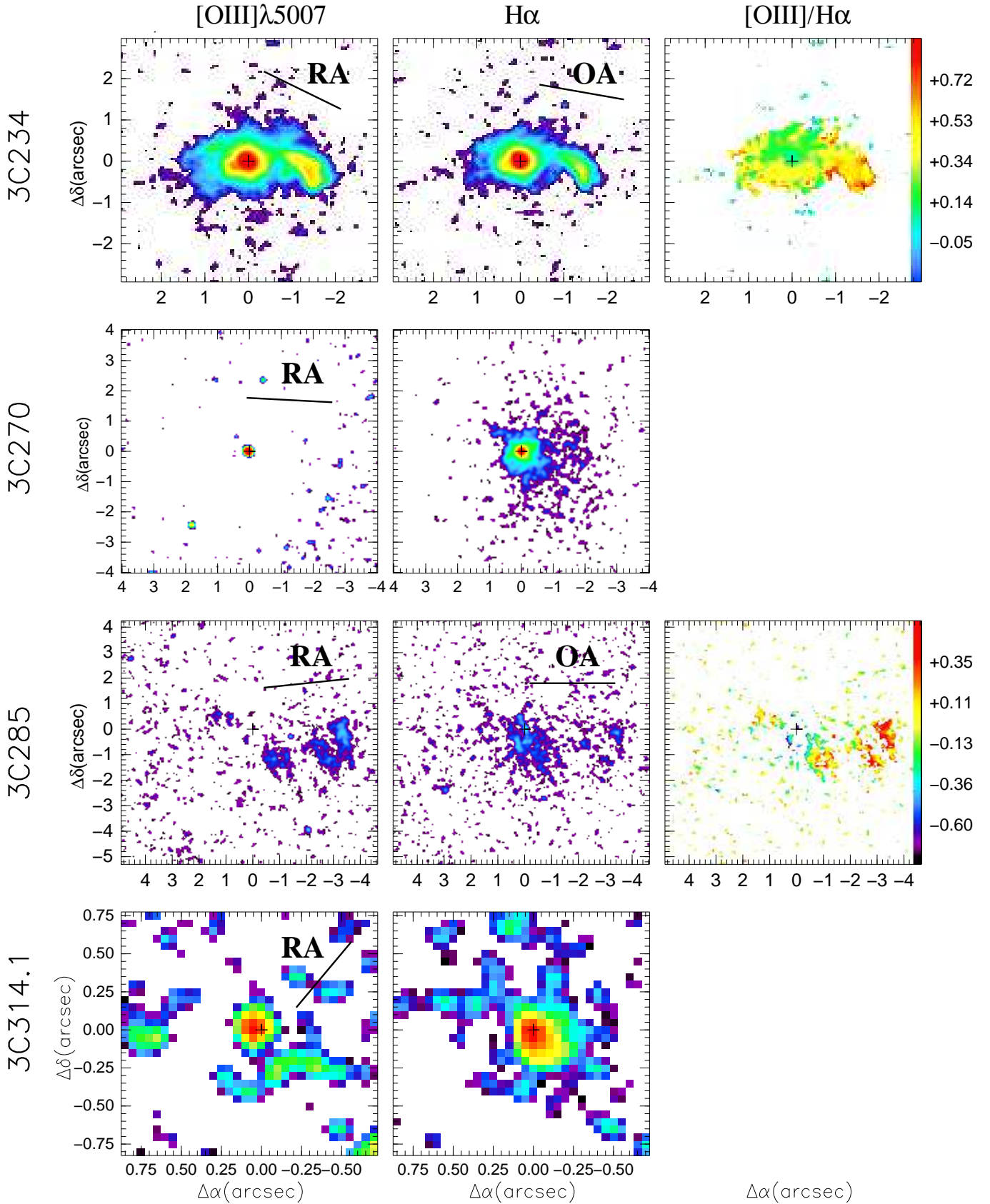


FIG. 2.— Continued

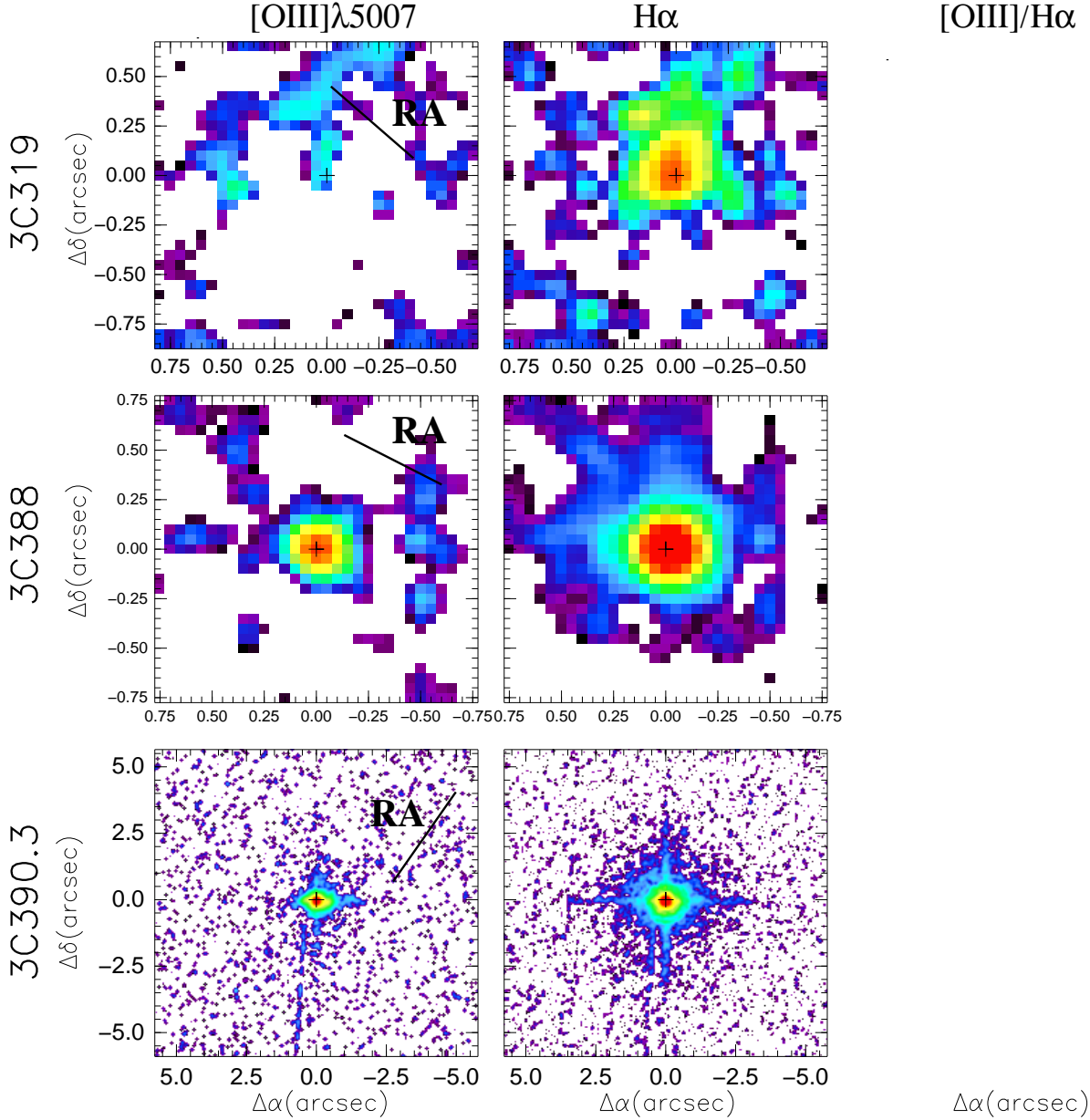


FIG. 2.— Continued

#### 4.2. Morphology and size of the ionized gas emission

The emission-line images in Figure 2 show a wide range of different morphologies. On one hand, HEGs show extended and disturbed morphologies on the scale of some kpc. Spectacular are the cases of 3C 33 and 3C 180. Their extended emission-line regions (ELRs) show tails, bridges, shells, irregular features and amorphous halos. The broad-lined HEG, BLOs, show more compact nuclear morphology. This is in line with the idea that the HEGs are the misaligned counterparts of the face-on BLOs (B09+). On the other hand, LEGs show less extended and compact morphologies (kpc or fraction of kpc) than HEGs. FR Is are generally more compact than FR IIs, since all FRIs are LEGs. Generally, H $\alpha$  and [O III] show similar structures. However, there are cases in which the morphologies of the two emissions are

substantially different. For example, the H $\alpha$  image of 3C 196.1 shows emission extended  $\sim 8$  kpc to the north-east of the nuclear region which is not observed in the corresponding [O III] image. Interesting are the cases of 3C 136.1 and 3C 196.1, which show two bi-conical structures of emission in the central region. A careful spatial comparison between the emission-line regions and the radio structures will be addressed in a forthcoming paper.

A straightforward way to measure the size of the NLR is to calculate the so called ‘flux weighted radius’ ( $R_{\text{flux}}$ ), using H $\alpha$  images, defined as:

$$R_{\text{flux}} = \frac{\sum_{\text{pix}} (F_{\text{pix}} \times d_{\text{pix}})}{\sum_{\text{pix}} F_{\text{pix}}} \quad (2)$$

where  $F_{\text{pix}}$  and  $d_{\text{pix}}$  are the flux of each pixel and the distance of the pixel to the center of the galaxy, indicated

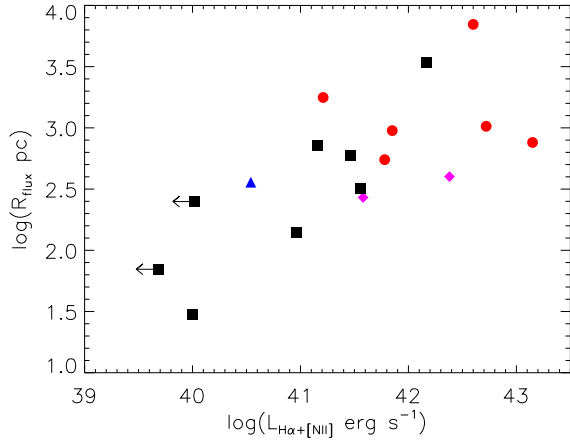


FIG. 3.— Comparison between  $R_{\text{flux}}$  and  $H\alpha$  luminosity for our sample. The black squares are LEG, the red circles are HEGs, the pink diamonds are BLOs and the blue triangle is the ELEG (3C 314.1).

with a cross in Figure 2. The values, presented in Table 3, range from 0.03 kpc in the case of 3C 129 to 7.00 kpc in the case of 3C 180, with a mean value for the whole sample of 0.55 kpc. The typical uncertainty on  $R_{\text{flux}}$  is  $\sim 22\%$ . HEGs have larger values of  $R_{\text{flux}}$  than LEGs, on average by a factor of  $\sim 2.3$ , but still consistent with each other within the errors. Figure 3 shows how the  $R_{\text{flux}}$  scales with the line luminosity for our sample. A clear trend  $R_{\text{flux}} - L_{H\alpha}$  is present, indicating that higher luminosity targets have larger ELRs.

To give an idea of the concentration of the emission, Figure 4 depicts the fraction of the  $H\alpha$  and the [O III] emission contained within the central kpc. The majority of the sample exhibits the line emission concentrated mostly in the inner 1 kpc. The fraction of the  $H\alpha$  line within the central kpc to the total  $H\alpha$  emission range from 0.07 to 1, with a median value of 0.64. In the case of [O III] the range goes from 0.04 to 1.0, with a median value of 0.87. The objects, which show large ELR emitting over 1 kpc, are HEGs, with the exception of one LEG, 3C 196.1. Regarding the HEGs, the  $H\alpha$  and [O III] emitted in the central kpc is roughly half than what is seen in LEGs in the same area. This means that LEGs typically show more compact emission-line region than HEGs.

#### 4.3. The [O III]/ $H\alpha$ line ratio images

The third column in Figure 2 depicts the log of the [O III]/ $H\alpha$  emission line ratios for those galaxies with extended emission and/or sufficiently high ( $> 5$ ) signal-to-noise (3C 33, 3C 93.1, 3C 136.1, 3C 180, 3C 196.1, 3C 197.1, 3C 219, 3C 234 and 3C 285). These sources are all FR IIs. They are all classified as HEGs (including 2 BLOs) except for one LEG (3C 196.1).

In the emission-line diagnostic diagrams (Kewley et al. 2006; Buttiglione et al. 2009), a net separation between LEGs and HEGs occurs by combining several narrow optical lines (e.g., [O III]/ $H\beta$ , [N II]/ $H\alpha$ ). Since we only studied [O III] and  $H\alpha$ , we cannot fully set up such diagnostics. However, these two lines can still separate the two classes although less sharply than the whole set of line ratios. Therefore, we used the [O III]/ $H\alpha$  ratios presented in the spectroscopic study of 113 3C radio sources

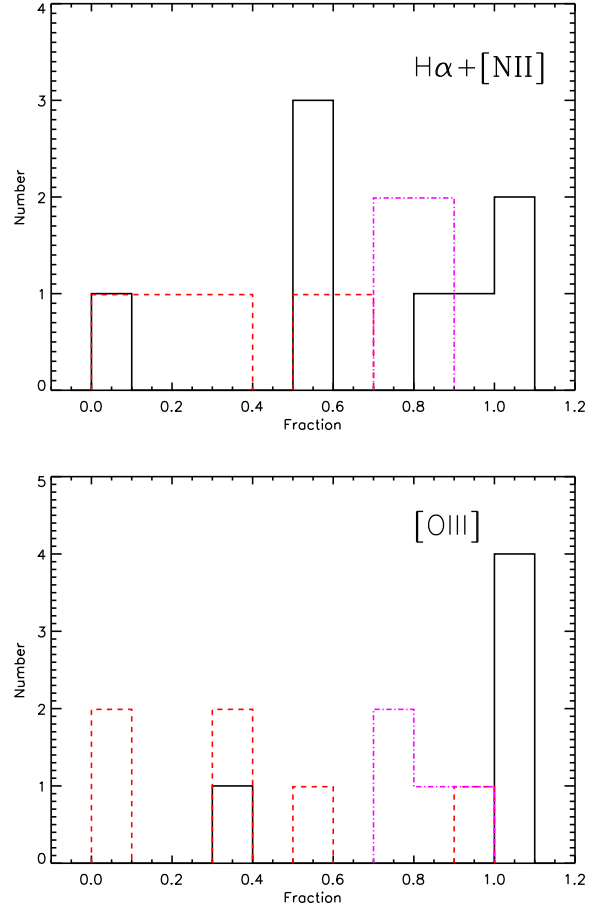


FIG. 4.— Histogram showing the detected fraction of the total  $H\alpha$  luminosity (upper panel) and [O III] luminosity (lower panel) within the central kpc. The black solid histogram stands for LEGs, the dashed red for HEGs, and the dot-dashed pink for BLOs.

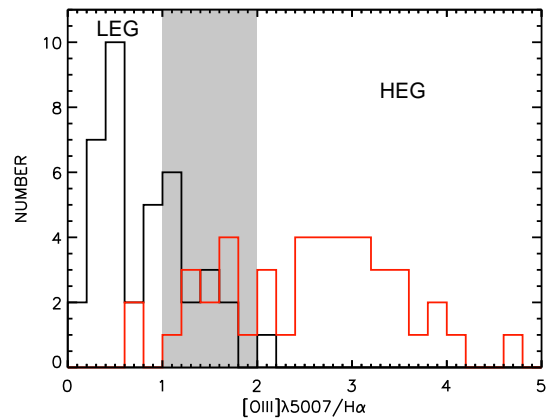


FIG. 5.— Histogram showing the [O III]/ $H\alpha$  distribution for the 113 3C radio sources in the (Buttiglione et al. 2009) sample. For the plot, BLOs were considered as HEGs. The black and red lines correspond to LEGs and HEGs respectively, and the grey-shaded region is the overlapping region where HEGs and LEGs share similar [O III]/ $H\alpha$  line ratios (1-2).

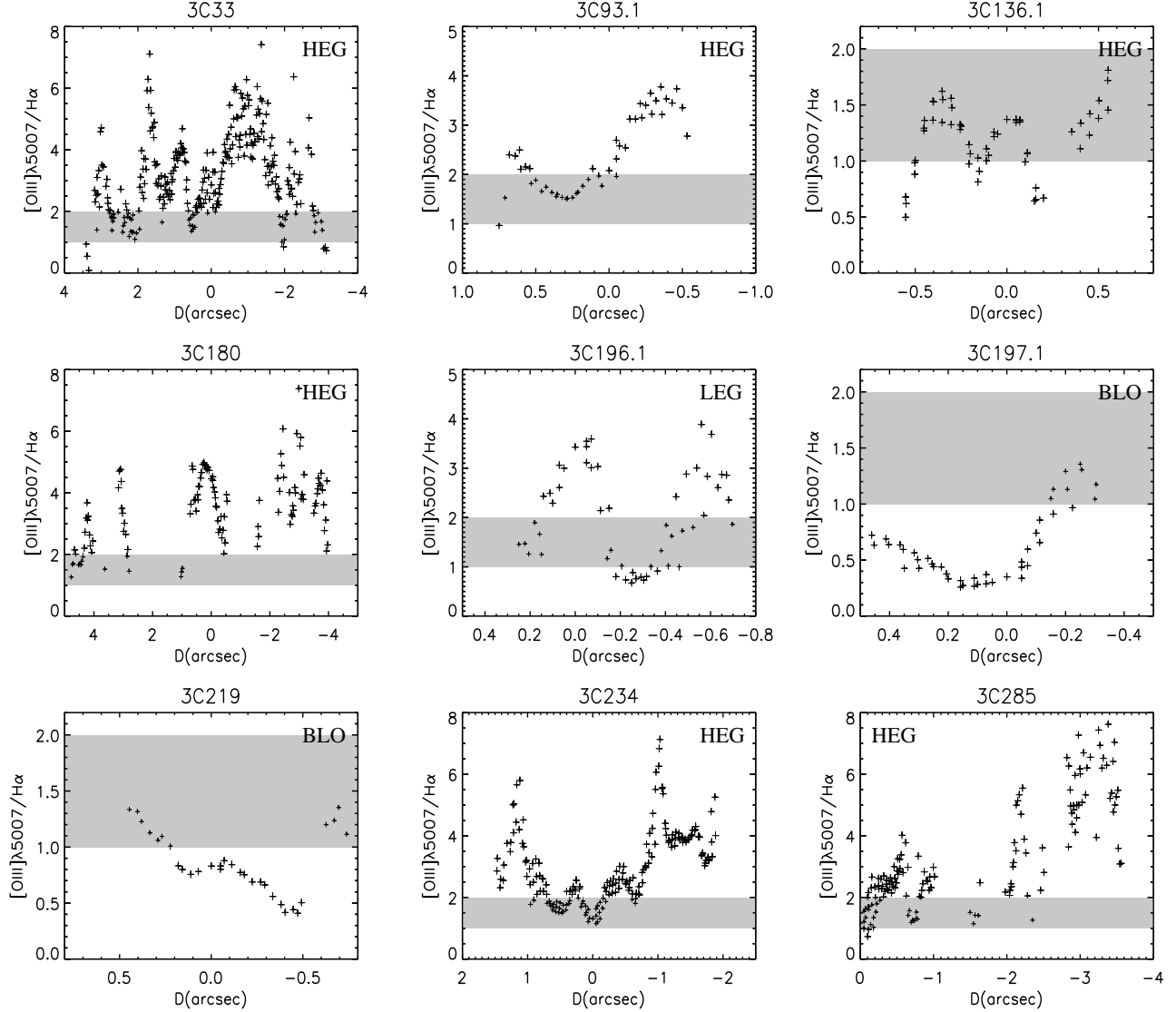


FIG. 6.— The  $[\text{O III}]\lambda 5007/\text{H}\alpha$  line ratios plotted against the distance from the nuclear region along the optical axis indicated in Figure 2. We used the values in Column 6 and 7 in Table 3 to account for  $[\text{O III}]\lambda 4959$  and  $[\text{N II}]\lambda\lambda 6949, 6983$  contribution to the flux in the band. The gray area corresponds to the range of  $[\text{O III}]\lambda 5007/\text{H}\alpha$  ratios, where LEG and HEG optical classifications overlap (see Fig. 5).

(B09+) in order to estimate the ‘typical’ line ratio values associated with HEGs and LEGs. Note that those ratios are taken from long-slit nuclear spectra. Figure 5 shows the histogram of the  $[\text{O III}]\lambda 5007/\text{H}\alpha$  of the 3C sample, where BLOs are naturally considered as HEGs. The black and red lines correspond to LEGs and HEGs respectively. As described above, a division between these two classes appears in the  $[\text{O III}]\lambda 5007/\text{H}\alpha$  ratio distribution, but with a broad overlapping region, shown by the grey-shaded area. HEGs and LEGs share similar  $[\text{O III}]\lambda 5007/\text{H}\alpha$  line ratios in the range of values 1 – 2 (0–0.3 in logarithmic scale). We use this range of ratios as reference to separate low- and high-excitation line ratios for our maps.

The emission line ratios maps in Figure 2 (third column) reveal that the  $[\text{O III}]\lambda 5007/\text{H}\alpha$  ratio may change across the ELR (between 0.2 and 5) from a LEG to HEG classification and viceversa. The ratio values shown to the right of the images are not corrected for either the  $[\text{N II}]\lambda\lambda 6549, 6583$  or the  $[\text{O III}]\lambda 4959$  contribution.

To quantitatively study the  $[\text{O III}]\lambda 5007/\text{H}\alpha$  ratio variation

across the galaxy, we opted for analyzing the line ratios along a preferential direction within the galaxy, for simplicity. This direction is the optical axis (marked as line and labelled as OA in Figure 2, central panels), defined as the axis crossing the center of the galaxy, along which the optical emission is more extended in either the  $[\text{O III}]\lambda 5007/\text{H}\alpha$  or the  $\text{H}\alpha$  images. Figure 6 plots the  $[\text{O III}]\lambda 5007/\text{H}\alpha$  line ratio values against the distance from the center of the galaxy, indicated with a cross in Figure 2 along the optical axis. In Section A.1 we performed a test to confirm the reliability of the plots showed in Figure 2 and Figure 6. The plots show a intense scatter pattern of the intensity ratio across the galaxy length, which reveal the large variation of the physical condition present in the ELRs on short scales.

When generating the plots in Figure 6, we correct the emission line ratio for  $[\text{O III}]\lambda 4959$  and  $[\text{N II}]\lambda\lambda 6949, 6983$  contribution to the flux in the band (see correction factor in Table 3), but not for reddening. In order to account for the effects of reddening, we examine the optical HST (F555W and F702W) WFPC2 images (Martel et al.

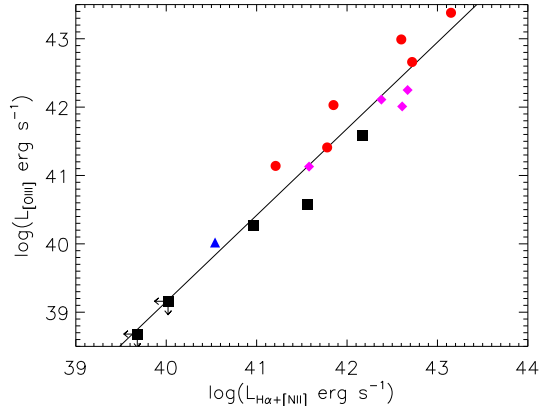


FIG. 7.— Log of the [O III] luminosity plotted against the log of the  $H\alpha$  luminosity for the 16 galaxies in our sample both measurements are available. The symbols are coded as in Fig. 3.

1999; de Koff et al. 1996) to search for dust features across the galaxies. We find that such components are evident in three of the galaxies in our sample, 3C 33, 3C 136.1 and 3C 285.

To further investigate the effects of dust on our emission line maps, we used the  $H\alpha$  and  $H\beta$  flux values from B09+ to calculate the  $H\alpha/H\beta$  ratio, which is sensitive to reddening. Assuming Case B recombination theory, this line ratio is  $\gtrsim 3$  if reddening is present. We found line ratios significantly higher than this value for three of the galaxies in our sample (3C 136.1, 3C 285 and 3C 319) due to the dimmed  $H\beta$ . For 3C 319 the spectrum is intrinsically weak and  $H\beta$  and [O III] are not detected, probably due not to absorption. Since dust attenuation is more important at shorter wavelengths, the [O III]/ $H\alpha$  line ratios presented in that figure for 3C 33, 3C 136.1, and 3C 285 can be considered as lower limits.

Two of the nine RGs included in Figure 6 (3C 197.1 and 3C 219) are classified as BLOs. Taking into account the contribution of the broad line in our emission-line images, estimated from nuclear spectra, their line ratios at the central location are underestimated by a factor of  $\sim 1.7 - 4$ .

The most interesting result is the variety of morphologies and sharp variations in the [O III]/ $H\alpha$  line ratio images, which are mainly observed in HEGs. Interesting is the case of 3C 33, two regions with [O III]/ $H\alpha$  line ratios of 4-8 are observed  $\sim 1.5''$  ( $\sim 1.7$  kpc) to the north-east and south-west of the nuclear region. 3C 180 shows line ratios of up to 8 spread through the filaments of emission observed 2-5'' (7-18 kpc) to the north and south of the nucleus. Another interesting case is 3C 234, where the highest line ratio values (6-8) are located at 1-2'' (3-6 kpc) to the west from the nuclear region.

Overall, HEGs show the highest line ratios ([O III]/ $H\alpha > 2$ ) and largest scatter even at large distance from the galaxy center (Figure 6). For the two BLOs and one LEG, the ratio variations are shallower.

#### 4.4. Luminosity correlations

In Figure 7 we compare the  $H\alpha$  and [O III] luminosities for the galaxies in our sample. A tight correlation is observed between the two emission lines in the form  $L_{[O III]} \propto (L_{H\alpha+[N II]})^{1.26 \pm 0.10}$ . We checked the statistical significance of such a trend by using a censored statisti-

cal analysis (ASURV; Lavalley et al. 1992) which takes into account the presence of upper limits. The rms of the residuals and the correlation coefficient are 0.35 dex and 0.96 respectively. If we correct the broadband images considering the [N II] and the second [O III] contribution from B09+ (Tab 3), a correlation is still present, with slope of  $1.19 \pm 0.14$ . The rms of the residuals and the correlation coefficient are 0.50 dex and 0.95 respectively. LEGs and HEGs lie on the same relation.

We also used our *HST*-ACS observations to test the already known correlation between the optical emission line luminosities and the 178 MHz radio power (Baum & Heckman 1989b,a; Rawlings et al. 1989; Rawlings & Saunders 1991; Morganti et al. 1992; Zirbel & Baum 1995). This is interpreted as a link between the AGN continuum emission and the mechanism of radio jet production (see Tadhunter et al. 1998, for a detailed discussion). Figure 8 shows the [O III] and the  $H\alpha$  luminosities plotted against the 178 MHz radio power (Table 2). We found correlations in the form  $L_{[O III]} \propto (L_{178\text{MHz}})^{0.52 \pm 0.3}$  and  $L_{H\alpha} \propto (L_{178\text{MHz}})^{0.70 \pm 0.2}$ , which are consistent with the correlations in the literature. The rms of the residual and the correlation coefficient are 0.70 dex and 0.81 for [O III] and 0.60 dex and 0.76 in the case of the  $H\alpha$  emission. When we correct for [N II] $\lambda\lambda 6549, 6583$  and [O III] $\lambda 4959$  contribution to the flux within the band, the correlation is still present with slopes of  $0.53 \pm 0.2$  and  $0.70 \pm 0.2$  for the [O III] and the  $H\alpha$  emission lines respectively. While HEGs and LEGs follow a common relation in Figure 8, Buttiglione et al. (2010) found different relations for the two classes. Although this discrepancy could be caused by the different integration area between our HST data and their nuclear slit spectra, the results of Buttiglione et al. (2010) on the almost-complete 3CR sample are, however, statistically stronger than what we found for 19 sources in this work.

Figure 9 provides an interesting result. It shows the 5-GHz radio core power (upper panel) and 2-10 keV X-ray nuclear luminosities (lower panel) in relation to the  $H\alpha$  luminosities of our sample. The two classes of objects, LEGs and HEGs, follow different linear correlations in these diagrams, in agreement with the results from Buttiglione et al. (2010). In fact, the probability that the two classes lie on the same correlations in the radio- $H\alpha$  and X-ray- $H\alpha$  planes is 10% and 32%, respectively. In the radio-core panel, the linear relations for LEG and HEG appear parallel ( $L_{core} \propto L_{H\alpha+[N II]}^\alpha$ , where  $\alpha$  is  $0.86 \pm 0.15$  for LEG and  $1.1 \pm 0.2$  for HEG and similar rms of  $\sim 0.7$  dex). The probabilities that the LEG and HEG radio-line correlations are fortuitous are, respectively 0.0006 and 0.0003. In the X-ray-line panel, the relations for the two classes are still distinct ( $L_X \propto L_{H\alpha+[N II]}^\alpha$ , where  $\alpha$  is  $0.3 \pm 0.2$  for LEG and  $0.95 \pm 0.30$  for HEG and similar scatter of  $\sim 0.7$  dex). The probabilities that the LEG and HEG X-ray-line correlations are fortuitous are, respectively 0.0008 and 0.0005. By correcting the line luminosities for [N II] $\lambda\lambda 6549, 6583$  and [O III] $\lambda 4959$ , the luminosity correlations are still valid with scatters and slopes consistent with the values reported above.

To test the correctness of the radio and X-ray luminosity correlations we found, we searched for the equivalent correlations in the flux-flux parameter space. The flux-

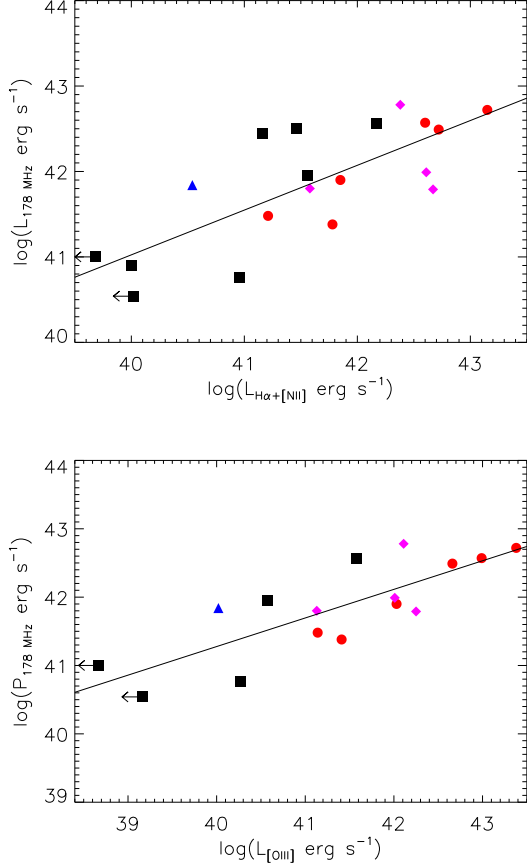


FIG. 8.— Radio power at 178-MHz plotted against the [O III] (upper panel) and the H $\alpha$  (lower panel) emission line luminosities. Symbols are the same as in Figure 3.

flux correlations are weaker than the luminosity correlations, but still statistically valid ( $<9 \times 10^{-4}$  of probability that a fortuitous correlation is present), given that the flux data scatters in the plots are slightly larger than those observed in Figures 8 and 9. In conclusion, all the correlations support the idea that the total amount of line emission produced on large scales for the two optical classes, LEGs and HEGs, depend on their different physical properties at nuclear scale.

#### 4.5. Photon budget, mass and covering factor of the ionized gas

In this section we calculate the ionizing photon budget for the emission-line regions and estimate the ionized gas masses and their covering factors for the RGs in our sample.

Assuming isotropic radiation from the central source, the number of ionizing photons,  $Q_{\text{ion}}$ , is obtained by integrating the luminosity density over the whole spectrum above  $\nu_0$ , which is the frequency corresponding to the ionization potential of hydrogen i.e:

$$Q_{\text{ion}} = \int_{\nu_0}^{\infty} \frac{L_{\nu}}{h\nu} d\nu \quad (3)$$

If we now assume a power law spectral shape in the form  $L_{\nu} = C (\nu/\nu_{\text{ref}})^{-\alpha}$ , where  $\nu_{\text{ref}}$  is any frequency for which the corresponding luminosity is known, equation 3 can be written as:

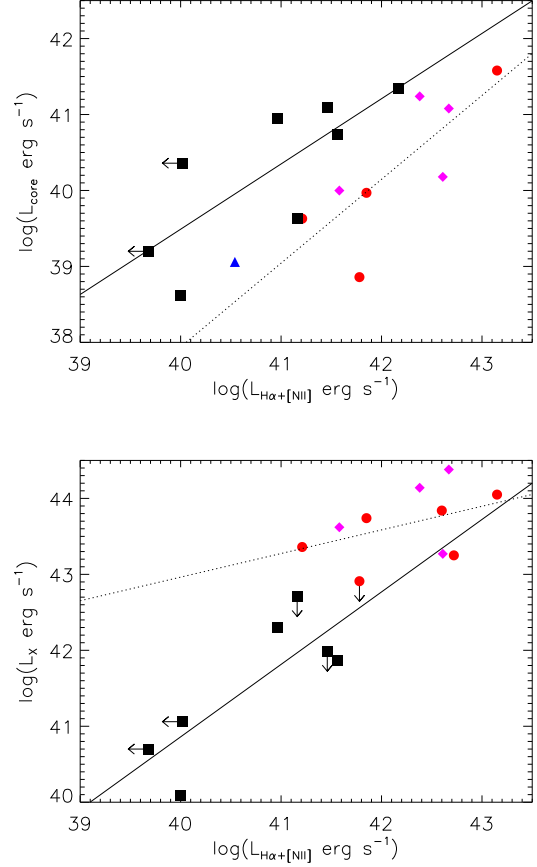


FIG. 9.— Radio core power at 5 GHz (upper panel) and X-ray intrinsic luminosities (2-10 keV) (lower panel) plotted against H $\alpha$  emission line luminosities. Symbols are the same as in Figure 3. The solid and dotted lines represent the best fits for LEGs and HEGs, respectively.

TABLE 4  
PROPERTIES OF THE IONIZING SOURCE AND IONIZED GAS

Name	$Q_{\text{ion}}$	$\Omega_{ELR}$	$n_e$	$M_{\text{ion}}$
3C	photon $s^{-1}$	(3)	$\text{cm}^{-3}$	$M_{\odot}$
(1)	(2)	(3)	(4)	(5)
33.0	$8.0 \times 10^{51}$	0.39	267	6.49
40	$1.7 \times 10^{49}$	$<0.62$	—	—
78	$3.2 \times 10^{50}$	0.28	—	—
93.1	$2.6 \times 10^{51}$	1.12	658	7.08
129	$2.0 \times 10^{48}$	1.03	606	4.58
132	$<3.7 \times 10^{51}$	$>0.08$	847	5.89
136.1	$<1.2 \times 10^{51}$	$>0.51$	606	5.92
180	$1.0 \times 10^{52}$	0.40	—	—
196.1	—	—	471	5.54
197.1	$5.6 \times 10^{51}$	0.37	806	5.28
219	$2.0 \times 10^{52}$	0.32	606	6.23
227.0	$2.6 \times 10^{51}$	1.8	606	5.79
234	$1.6 \times 10^{52}$	0.9	328	7.70
270	$9.4 \times 10^{49}$	$<0.05$	—	—
285	$3.6 \times 10^{51}$	0.15	10	7.32
314.1	—	—	—	—
319	$<7.5 \times 10^{50}$	$>0.19$	451	5.78
388	$1.2 \times 10^{50}$	1.05	381	5.74
390.3	$3.6 \times 10^{52}$	0.33	606	6.11

NOTE. — Col (1): 3C Name. Col (2): number of ionizing photons  $Q_{\text{ion}}$ . Col (3): covering factor. Col (4): electron densities estimated using the [S II]6716/6731 line ratios from integrated optical spectra (Buttiglione et al. 2009, 2010). Col (5): ionized gas mass.



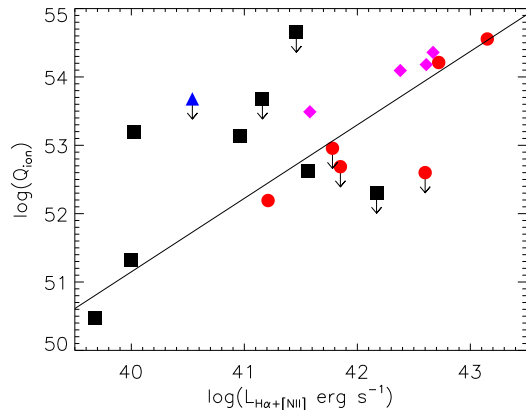


FIG. 10.—  $H\alpha$  luminosity vs number of ionizing photons estimated in the X-ray (2-10 keV) band. Symbols are the same as in Figure 3. Using a censored statistical analysis, a tentative trend is observed whose slope coefficient is  $1.08 \pm 0.25$ .

$$Q_{ion} = \frac{C}{h\alpha} \left( \frac{\nu_0}{\nu_{ref}} \right)^{-\alpha} \quad (4)$$

where the constant  $C$  is the normalization of the spectrum. The ionizing photons are produced in two main regions of the electromagnetic spectrum, in the UV-optical and X-ray range. The UV-optical nuclear luminosities of HEGs (Chiaberge et al. 2002a,b) would significantly underestimate their real photon budget because their nuclei are obscured, partially obscured or dominated by scatter emission (Baldi et al. 2010, 2013). Conversely, hard-X-ray luminosity (2-10 keV) is a better proxy to estimate the number ionizing photons than the UV-optical band, because less effected by obscuration.

Therefore, we derived the  $Q_{ion}$  from the X-ray wavelengths. In order to determine the value of the constant  $C$ , and hence the number of ionizing photons, we use the 2-10 keV X-ray luminosities and photon indexes  $\Gamma$  ( $\Gamma = \alpha + 1$ ) for the galaxies in our sample from Torresi et al. (in prep) (using *Chandra* data, Table 2) as follows:

$$L_{X-ray} = \int_{2keV}^{10keV} L_{\nu} d\nu \quad (5)$$

The number of ionizing photons in the X-ray band are shown in Table 4. Figure 10 displays the  $H\alpha$  luminosities versus the total number of ionizing photons,  $Q_{ion}$ . A monotonic, weak trend between the two quantities appears (probability that a fortuitous correlation appears is 0.0035). This indicates that the AGN primarily provides the ionizing photons to account for the emission-line luminosities for our sample of RGs.

We estimate the covering factors of the ELRs,  $\Omega_{ELR}$ , by using the  $L_{H\alpha}$  from our maps. In the case of low-density NLR clouds, in case-B recombination, the number of ionizing photons can be related to the  $H\alpha$  luminosity in the form (Osterbrock 1989):

$$\frac{L_{H\alpha}}{2h\nu_{\alpha}} = \frac{\Omega_{ELR} Q_{ion}}{2.2} \quad (6)$$

Assuming a bolometric 2-10 keV correction factor of 30 (Vasudevan et al. 2010; Lusso et al. 2012) to correct the ionizing photon budget, we measure the covering factors

of our sample, presented in Table 4.  $\Omega_{NLR}$  range between  $\sim 0.05$  and 1.8 with a mean value of 0.66. Four sources (3C 93.1, 3c 129, 3C 227, 3C 388) show covering factors larger than unity. LEGs show slightly smaller mean covering factors (0.60) than HEGs and BLOs (0.71), but the difference is not statistically significant ( $P < 90\%$ ).

As discussed in Osterbrock (1989), we can use the  $H\alpha$ -line luminosity to estimate the mass of the ionized gas for the galaxies in our sample using the expression:

$$M_{ion} = \frac{L_{H\alpha} m_p}{\alpha_{H\alpha}^{eff} h\nu_{\alpha} n_e} \quad (7)$$

where  $m_p$  is the the mass of the proton,  $\alpha_{H\alpha}^{eff}$  is the  $H\alpha$  recombination coefficient ( $1.17 \times 10^{-13} \text{ cm}^3 \text{ s}^{-1}$ ) and  $n_e$  is the electron density. To estimate  $n_e$ , we use the  $[S II]\lambda\lambda 6716, 6731$  emission line ratio<sup>6</sup>, obtained from the optical spectra (B09+). Table 4 presents  $n_e$  for the galaxies in our sample and the corresponding ionized gas mass estimates,  $M_{ion}$ . In the cases of 3C 78 and 3C 270 it is not possible to obtain adequate  $[S II]\lambda\lambda 6716, 6731$  measurements. For 3C 40, 3C 180 and 3C 314.1 the  $[S II]6716/6731$  line ratios are outside the low density limit (1.52). We obtain a wide range of electron densities ( $10 - 806 \text{ cm}^{-3}$ ) with a median value of  $606 \text{ cm}^{-3}$ . These values give ionized gas masses ranging from  $3.8 \times 10^4$  to  $5.0 \times 10^7 M_{\odot}$ , with a mean value of  $6.6 \times 10^6 M_{\odot}$ . The interesting result is that HEGs have more massive ELRs than LEGs by a factor of  $\sim 8.5$ . Note that the  $[S II]$  ratio is estimated in the nuclear region and probably not representative of the conditions in the outer region of the ELR. Consequently, for a more tenuous ELR, this approach might lead to an underestimation of the actual ionized gas masses.

#### 4.6. Radio – optical alignment

In this section we qualitatively study the radio and optical alignment for our sample. A detailed spatial superimposition of the radio and emission-line region maps will be presented in a forthcoming paper.

The black-solid lines drawn in the  $H\alpha$  images in Figure 2 show the orientation of the optical axis. It is defined as the angle between the optical axis (defined in Sect 4.4) and the North direction. There are eight sources (3C 129, 3C 132, 3C 219, 3C 270, 3C 314.1, 3C 319, 3C 388 and 3C 390.3) in which the relatively low signal-to-noise and/or the amorphous morphology of the detected emission makes the definition of an optical axis rather arbitrary. Therefore, for these eight sources no optical axis is shown in Figure 2. In addition, the radio axes of the galaxies based on high-resolution VLA images (jet position angle, de Koff et al. 1996; Martel et al. 1999; Privon et al. 2008 and references therein) are plotted in Figure 2 onto the  $[O III]$  images.

Figure 11 describes the radio axis plotted against the optical axis for the eleven sources in our sample with the two measurements available. The main result is that the two axes have similar orientations. This suggests that the optical emission is tightly related to the radio emission, as expected by the the 'alignment effect' observed in RGs. The source which shows the largest radio/optical axis

<sup>6</sup> We used the *TEM DEN* IRAF routine to compute electron density from diagnostic line ratios.

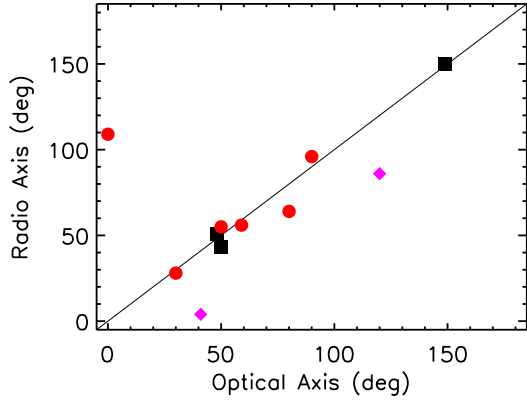


FIG. 11.— Radio axis plotted against the optical axis (N is  $0^\circ$  and E is  $90^\circ$ , see text for details). The values are in degree. The symbols are coded as in Fig.3.

TABLE 5  
COMPARISON BETWEEN LEGS AND HEGs

quantity	sample	LEG	HEG	units
$\log L_{H\alpha}$	$41.58 \pm 0.23$	$40.85 \pm 0.30$	$42.26 \pm 0.18$	$\text{erg s}^{-1}$
$\log L_{[O III]}$	$41.31 \pm 0.34$	$39.96 \pm 0.51$	$42.11 \pm 0.23$	$\text{erg s}^{-1}$
$R_{flux}$	$1.09 \pm 0.41$	$0.69 \pm 0.37$	$1.59 \pm 0.74$	kpc
$\Omega_{ELR}$	$0.66 \pm 0.13$	$0.60 \pm 0.17$	$0.71 \pm 0.17$	—
$\log M_{ion}$	$6.82 \pm 0.21$	$5.67 \pm 0.21$	$7.00 \pm 0.25$	$M_\odot$

NOTE. — Mean values of the physical quantities with  $1\sigma$  errors obtained for the entire sample and the two optical classes, LEGs and HEGs. We used the Kaplan-Meier estimator to derive the mean values by considering the censored data with ASURV package.

discrepancy is 3C 136.1 which shows a bipolar emission-line structure, transversal to the jet.

## 5. DISCUSSION

Our results on the HST images of local RGs point towards the active nucleus as the main driver of the emission-line properties we observe. We note a different behavior between the ELR properties of the AGN populations, HEG and LEG, in our sample: larger sizes, masses, luminosities in favor of HEGs (Table 5 summarizes the mean values of the two classes for comparison). Generally for our radio sample, higher line luminosities are associated with larger ELRs, in agreement with the size-luminosity dependence found for Seyferts and QSOs (Fischer et al. 2018).

Morphologies and luminosities of the ELRs are consequences of two factors: the source of ionizing photons and the available content of cold gas in the ISM. These two elements are not completely disjointed since AGN feedback on the host and gas accretion on the BH are mutually regulated processes. In the next sub-sections we discuss the topic of emission-line gas in RG, addressing the ionization mechanism and the gas properties, in the framework of the two classes of radio-loud AGN, LEG and HEG, which are known to correspond to two different accretion modes, hot and cold, respectively (e.g. Best & Heckman 2012).

### 5.1. Ionization mechanism

Early studies clearly show that the optical emission-line gas is ionized by the nuclear continuum,

whose properties are set by the central engine (e.g. Baum & Heckman 1989a; Rawlings & Saunders 1991). The relation of the line emission with the radio jet power indicates that its kinetic energy deposited in the ELR has an important contribution in the energy budget of the photoionization of the clouds, independently of the AGN class. Linear correlations found between the emission-line luminosity and the nuclear activity indicators, such as X-ray and radio core luminosities (Figures 8 and 9), confirm this scenario. However, those correlations clearly indicate a discrepancy between LEGs and HEGs. The HEG population shows an excess of emission line luminosity of a factor  $\sim 10$  with respect to the LEGs, when matched in radio core luminosities. Such a line excess is indicative of an additional ionizing component to the radio jet. Instead, in the X-ray–line plane, the two classes occupy different regions of the diagram, with HEGs more luminous in general than LEGs, suggesting two different main ionizing mechanisms responsible to the line properties of the two populations.

Many recent multi-band studies indicate a bi-modality in the accretion modes for RL AGN. In turn, such a behavior corresponds to a bi-modality in the ‘*ionization modes*’. For the LEG population (the hot-gas accretors), the synchrotron radio emission from the jet is enough to account for their multi-wavelength properties: X-ray, UV, optical, IR and line luminosities correlate with the radio core, which is a proxy of the jet energetics (e.g., Balmaverde et al. 2006; Balmaverde & Capetti 2006; Chiaberge et al. 1999, 2002a; Capetti et al. 2005; Baldi et al. 2010; Hardcastle et al. 2009 and other references therein). Conversely, HEGs (the cold-gas accretors) systematically exhibit an excess with respect to the synchrotron-jet component, which is ascribed to the standard accretion disk to account for their higher multi-band and line luminosities than the LEGs. Our results point to a linked bi-modality, accretion vs. ionization. On one hand, the picture of a radio jet illuminating the NLR of LEGs fits the previous multi-band studies. On the other hand, the accretion disk provides further ionizing photons to irradiate the ELR of HEGs.

Once the radiation field is produced either by the jet or the accretion disk, the ISM in the host galaxies reprocesses the ionizing light into emission lines depending on their available cold gas amount. The dust and cold gas present in a large amount in HEGs are visible in the optical band and detected either in the IR band or in molecular lines ( $10^7$ – $10^8 M_\odot$ , Baldi & Capetti 2008; Smolčić & Riechers 2011; Tadhunter et al. 2014; Westhues et al. 2016). These are usually tracers of the location of the emission-line gas (Dicken et al. 2009). Conversely, LEGs are typically hosted in red gas-poor, passively evolving ETGs (Baldi & Capetti 2008; Smolčić 2009; Prescott et al. 2018), which justify their small sizes and moderate masses of the emission-line gas. The combination of the harder quasar radiation field, powerful jets and the larger amount of gas accounts for their larger ELR sizes and luminosities of HEGs than LEGs.

However, is the AGN continuum (accretion disk and jet) really enough to account for the emission line properties we observe? Different specific aspects of the ionized gas suggest that other sources of high-energy photons may contribute to the photoionization of the gas.

The presence of tails, bridges, shells, irregular features

and amorphous halos observed in the emission-line maps of some HEGs (3C 33, 3C 180, and 3C234) are suggestive of traversal jet interaction with the ISM. The outward motion of the radio jet may result in the passage of shocks through the clouds. The shock occurs at the interface between the outflowing plasma and the ambient medium, such as in the hot spots and on the lateral edges of the jet cocoon, a crucial site of gas photoionization. Couto et al. (2017) observed increased line ratios for 3C 33 outwards, using Integral field spectroscopy with Gemini, and interpreted them as due to a lateral expansion of the ambient gas in the nuclear strip due to shocks produced by the passage of the radio jet. Supernovae and past radio outbursts can also produce multiple shocks through the ISM and cause line-emitting regions cospatial with the radio emission (e.g., Rampadarath et al. 2018). In the case of our emission maps, the region of multiple shocks is clear for 3C 180, where at the edges of the radio lobes, the gas is pressured and ionized. These emission features are more common for FR IIs because they have larger jet bulk speeds and larger radio lobes than FR Is. This difference would contribute to explain why FR IIs (and then HEGs) show more extended and variegated morphologies of ionized gas than FR Is.

Another source of high-energy photons are the young, hot stars. Robinson et al. (1987) concluded that the very extended emission-line gas in RGs can be photoionized by typical O and B stars. The extended disturbed patches of ionized gas observed in 3C 33, 3C 234 and 3C 285 seem to be associated with regions of intense star formation, induced by jet shocks or by a tidal merger/interaction, as suggested by the HST images (Madrid et al. 2006; Floyd et al. 2010; Baldi & Capetti 2008). These sources are all classified as HEGs. Indeed, this ionization mechanism may contribute more for the HEGs which show evidence of ongoing star formation rather than more passive host galaxies of LEGs (e.g., Baldi & Capetti 2008, 2010; Herbert et al. 2010; Janssen et al. 2012; Hardcastle et al. 2013; Gürkan et al. 2015; Westhues et al. 2016). Post-AGB stars which also emit in UV can also play a minor role in the photoionization.

### 5.2. Covering factor

The mean covering factor we measured from the HST images for our objects, 0.66, is in agreement with the broad range of values derived from previous multi-band studies for radio-quiet and -loud AGN in the same interval of nuclear luminosities (0.1–0.8, e.g. Netzer & Laor 1993; Wills et al. 1993; Maiolino & Rieke 1995; Zheng et al. 1997; Laor et al. 1997; Maiolino et al. 2001; Capetti et al. 2005). This result also reconciles with the relative weakness of the NLR with respect to the BLR, typically 0.1–0.01 per cent (Boroson & Green 1992; Osterbrock & Shuder 1982; Osterbrock 1989; Buttiglione et al. 2009).

We also estimated covering factors larger than the unity for four sources, belonging to both LEG and HEG populations. This result indicates that the line emission measured from the HST images is larger than what we expected from the ionizing photon budget. Different aspects might cause an overestimation of the covering factors. A systematic larger error of the line flux density for a partially incorrect continuum subtraction in the bandwidth can affect our  $\Omega_{\text{NLR}}$  estimates.

The underestimation of the power of other contributing ionizing sources, i.e. jet shocks and star formation in the ISM in the outer region of the ELR, can lead to a low photon ionizing budget. A small change in the X-ray spectral index or the bolometric correction factors, which are known to vary broadly for different AGN classes (Ho 2008; Lusso et al. 2012), could lead to a significant change in the estimation of the photon budget  $Q_{\text{ion}}$ . The assumption of the isotropy of the ionizing nuclear source might have an effect on the covering factors. Marginal effect on the  $\Omega_{\text{NLR}}$  could come from relativistic beaming in optical nuclei (Capetti et al. 2005) and X-ray nuclear variability.

Overall, our study shows that HEGs have slightly larger covering factors than LEGs, despite consistent within the errors. In line with our results we found for the two populations, this  $\Omega_{\text{ELR}}$  difference can be interpreted as due to the the combined effect of the stronger central engine and larger availability of cold gas, valid for HEGs.

### 5.3. $[O\ III]/H\alpha$ across the galaxy and feedback

The emission-line ratios depend on both the gas density and the gas proximity to the ionizing source (e.g. Jackson & Rawlings 1997; Kewley et al. 2006). Therefore, one would expect low-excitation lines such as  $H\alpha$  to be present at larger scales in the galaxy with respect to high-excitation lines, such as  $[O\ III]$ . However, for at least 5 ( $\sim 26\%$ ) galaxies in our sample, all HEGs (3C 33, 3C 180, 3C 227, 3C 234, 3C 285),  $[O\ III]$  extended emission is clearly observed at larger scales (on kpc scale) than that of  $H\alpha$ . These results are similar to previous studies on ELR in radio-quiet and -loud galaxies (Robinson et al. 1987; Storchi-Bergmann et al. 1996; Capetti et al. 1996; Robinson et al. 2000; Taylor et al. 2003; Kraemer et al. 2008; Maksym et al. 2016). The observed line ratios are consistent with the idea of a mixed medium, with a variegated density and optical depth even at large distance from the central BH illuminated by various ionizing sources along the optical axis (e.g. Binette et al. 1996).

Furthermore, larger amplitude variations of the  $[O\ III]/H\alpha$  ratios have been observed across the extension of the ELR for HEGs, rather than for LEGs (Fig. 8). Therefore, in light of our results, how can we explain this high  $[O\ III]/H\alpha$  at large distance from the ionizing nucleus and large variation of this ratio? Different scenarios might account for the observed ratios.

It is possible that the lack of extended  $H\alpha$  emission compared to that of  $[O\ III]$  is related to the sensitivity of our *HST* observations. For example, in the case of 3C 227, our images show faint extended  $[O\ III]$  emission (over 20 kpc) towards the southeast of the galaxy that is not visible in the corresponding  $H\alpha$  image. However, the same structures are clearly visible in both the  $[O\ III]$  and  $H\alpha$  images of the galaxy studied by Prieto et al. (1993).

Another possibility is an inadequate correction of  $[N\ II]\lambda\lambda 6549, 6583\text{\AA}$  emission lines to the flux within the bandpass of filter used to image the  $H\alpha$  emission. This is due to the fact that  $[N\ II]$  line may change across the spatial extent of the galaxies. In fact, long-slit spectroscopic studies along the NLR reveal line ratio  $H\alpha/[N\ II]\lambda\lambda 6949, 6983$  changes by a factor of 1.0 - 5.3 from the nuclear to the extended regions of the galaxies

(e.g. Robinson et al. 1987; Storchi-Bergmann et al. 1996; Robinson et al. 2000; Taylor et al. 2003). Therefore, assuming that a similar change occurs in our maps, this effect would overestimate the [O III]/H $\alpha$  line ratios by a factor of  $\sim 2$  at large scales. This effect might be important for galaxies with substantial extended emission, such as HEGs.

Another factor which might affect the [O III]/H $\alpha$  ratio is the reddening. Due to dust mostly in the central regions, the H $\alpha$  emission at large distance should be less affected than the [O III] emission. This is the case for 3C 33, 3C 136, and 3C 285 which show dust features across the optical galaxy and decoupled [O III] and H $\alpha$  emission in our maps.

Assuming the observed line ratio scatters are real, physical scenarios can be discussed in the framework of feedback processes. Both anisotropic AGN illumination and jet-cloud interaction, which produce radiation continuum over a wide range in ionization parameters, can account for the ionization states of both the nuclear and the off-nuclear emission line gas (Robinson et al. 1987; Tadhunter et al. 2002). In the context of a quasar-mode feedback, theoretically, a standard-disk ionizing continuum, which probably includes combination of power-laws, thermal bumps, a high-energy tail and outflowing gas (Binette et al. 1988), predicts the observed strengths of high-ionization lines, mainly [O III] (Robinson et al. 1987). This ionizing source can also explain the large [O III]/H $\alpha$  observed across the galaxy in HEGs. The kinetic energy released by the jets and shocks are important sources of ionizing photons in RGs, for both the AGN classes. The local kinematics and the gas pressure, in an event of gas expansion due to the jet passage, should be considered since they surely play a role in the photoionization mechanism (see the integral field spectra of 3C 33 Couto et al. 2017). Shocks can mimic the emission line ratios typical of a LEG (Allen et al. 2008; Best et al. 2000). Furthermore, different sources of high-energy photons located across the galaxy extension, might provide further ionization at large distances from the center. Sparse knots of star formation and post-AGB stars, can produce a substantial diffuse field of ionizing photons: the resulting emission line ratios cover the whole region typical of LEGs and HEGs in the diagnostic diagrams (Binette et al. 1994; Stasińska et al. 2008; Sarzi et al. 2010). In conclusions, all the various sources of energetic photons present across the galaxy have an important impact on the multi-phase gas of the galaxy (positive and negative feedback, Morganti 2017; Cresci & Maiolino 2018) and contribute to the large scatter observed in [O III]/H $\alpha$  maps.

The combination of the primary central quasar with the jets and the secondary ionizing sources located along the optical axis, would explain the large emission-line ratio variation observed in our maps of the HEG population. Conversely, the lack of star formation and of a bright quasar makes the emission line morphologies of LEGs more homogeneous and neat. The LEG population of our sample fits in a more simple picture where the synchrotron photons mainly ionize the surrounding gas and account for the small scatter observed in the [O III]/H $\alpha$  ratios. Old stellar population, tracing the smooth elliptical galaxy, might marginally contribute to ionize the gas in the central region of the host.

## 6. SUMMARY AND CONCLUSIONS

We have presented HST/ACS narrow-band [O III] and H $\alpha$  images for a sample of 19 RGs with redshifts  $< 0.3$ . We studied the morphology of the emission-line regions and the ratio between the two lines. Based on the emission-line ratios from nuclear long-slit spectra, we divided the sample into HEGs and LEGs, which are known to have two different accretion modes: cold-gas and hot-gas accretors, respectively. The line properties and the linear correlation between radio core power, X-ray luminosities and the total emission line luminosities suggest two different pictures for the two classes:

- LEGs show more compact ELR on scale of kpc but smaller than HEGs. The mean covering factor is 0.60 associated with ionized masses of  $4.7 \times 10^5 M_{\odot}$ . The variation of the [O III]/H $\alpha$  ratio across the ELR is smaller than the sharp changes observed for HEGs. All these properties of ELR reconcile with a picture of a LEG, powered by a synchrotron-dominated nucleus. In fact, the main source of high-energy photons is the radio jet, which ionize a secular gas-poor environment.
- HEGs produce more prominent ELR properties than LEGs. Their structures are more extended, on scale of some kpc, and more disturbed than LEGs line regions. The covering factors are slightly larger than LEGs and the involved ionized masses are larger, up to  $10^{7.70} M_{\odot}$ . The [O III] gas is observed also at large distances from the nucleus, making the [O III]/H $\alpha$  ratios change rapidly across the ELR. All these properties of their ELR match with the picture of HEGs, powered by a quasar (standard accretion disk), which contributes to illuminate the gas-rich ISM together with the radio jets. However, to justify the emission-line ratio changes and the morphologies, we need to invoke further photoionizing sources. Star-formation and shocks from the radio jets contribute to the photoionization of the clouds along the radio/optical axis.

Based on our current comprehension of the radio AGN phenomenon (e.g. Best & Heckman 2012; Heckman & Best 2014), we can put our results into the following galaxy-AGN evolutionary scenario: a link between the accretion and the photoionization modes valid for radio-loud AGN is emerging. On one hand, LEGs, which live in rich environments (Hardcastle 2004; Tasse et al. 2008; Ramos Almeida et al. 2013; Gendre et al. 2013; Castignani et al. 2014; Ineson et al. 2015), have gone through a 'dry' merger process (Balmaverde & Capetti 2006) in the past, lacking dust and a cold gas reservoir. The paucity of such a gas prevents the formation of a radiatively efficient accretion disk. The radio jet, sustained by the hot-phase accretion, is the main source of ionizing photons, sufficient to account for the compact weak line regions observed in LEGs. On the other hand, HEGs have been recently engaged in galaxy-galaxy interaction/mergers ('wet' merger) (Baldi & Capetti 2008; Ramos Almeida et al. 2011, 2012; Herbert et al. 2010; Hardcastle et al. 2013; Chiaberge et al. 2015), which bring new fresh cold gas

and can trigger either star formation and/or cold-gas accretion. This cold gas reservoir feeds the standard accretion disk, which in turn supports the launch of powerful jets. These ionizing sources mainly illuminate the NLR, creating bright extended disturbed emission line morphologies, as observed in our HST maps. Their line morphologies also resemble their optical-UV galaxy disturbances (Baldi & Capetti 2008), suggestive of an ISM which has not settled down yet after the merger. Star formation across the galaxy and shocks might contribute to the photoionization at large distances from the nucleus.

The positive feedback of the jet and the central AGN on the ISM are also supported by the alignment of the radio axis with the morphology of the ELR. While what expected from a radio-mode feedback matches the emission-line properties of the LEGs, the quasar-mode feedback plays a crucial role to interpret the ELR properties of HEGs, similar to what observed in local radio-quiet Seyferts/QSO (Williams et al. 2017; Fischer et al. 2018; Revalski et al. 2018). In both the feedback modes, the gas is photoionized along the axis of the jet, where most of the ionizing photons are able to escape and most of the cold gas is shocked. Hydrodynamic models of jet expansion in a two-phase ISM, which predict double or multiple bubbles with velocity fields ranging between 500 and 1000 km s<sup>-1</sup>, indicate that the kinetic energy of this outflow transfers from 10% to 40% of the jet energy to the cold and warm gas (Wagner et al. 2012), resulting in gas ionization along the radio jet. A radio-mode feedback is equally important for LEGs and HEGs (Whittam et al. 2018). However the AGN illumination needs to be also taken into account to interpret the ELR properties of HEGs. The interplay between bulk flow and turbulence from a jet and the bi-conical illumination from a quasar, are important aspects to stir up and photoionize the ISM,

predicting broadly the disturbed morphologies and properties of the ELR for HEGs.

We estimated a mean emission-line covering factors of 0.66 for our sample. The marginally larger covering factors found for HEGs than LEGs is probably the result of the different conditions present in the hosts of two classes. In the case of LEGs, the paucity of cold gas and the weaker radiation field produced by the jet result in smaller covering factors. As observed in nearby Seyferts (e.g. Contini et al. 2012; Villar Martín et al. 2015; Freitas et al. 2018), a radiation-bound photoionization model from the AGN, outflow, jet shocks and young stars and the large amount of gas clouds support the extreme line properties observed in HEGs and the larger covering factors (Hainline et al. 2014; Dempsey & Zakamska 2018).

The advent of the high-resolution integral field era, i.e. VLT/SINFONI and MUSE, is bringing interesting results on the study of jet-ISM interplay in local galaxies (e.g., Santoro et al. 2015; Dasyra et al. 2015; Cresci et al. 2015; Salomé et al. 2016; Roche et al. 2016; Balmaverde et al. 2018). However, the AGN feedback is still an appealing and complex phenomenon, on which this new era of telescopes will cast more light to understand this mechanism in the next future.

The authors wish to thank A. Laor for the insightful discussion, E. Torresi for providing the X-ray spectral analysis of the sample, and D. R. A. Williams for the helpful comments on the line properties of the sample. We also thank the reviewer for the useful comments, which helped us improve the quality of the manuscript. RDB and IMC acknowledge the support of STFC under grant [ST/M001326/1].

## APPENDIX

### A.1. CONTROL CHECK OF THE [O III]/H $\alpha$ SPATIAL DISTRIBUTION

To test the potential effects of misalignment and/or low signal-to-noise of the two emission-line ratio maps, we first shift the narrow band images prior to the continuum subtraction using 0.5 and 1 pixel shifts in each direction, x and y. Secondly, the [O III] and the H $\alpha$  images are binned using a 2  $\times$  2 pixel binning mode with the aim of increasing the S/N and reduce the effects of any small mismatch. An example of the ‘2  $\times$  2 binning’ test is shown in Figure 12 using 3C 180. The plots corresponding to each galaxy shown in Figure 6 are generated after each of these tests. Although the individual values of each pixel changed, the general trends remain the same.

The [O III]/H $\alpha$  images of the galaxies are systematically observed using the same chip and the same pointing set up, within the same orbit and using the same guiding star. Therefore, if the contribution of the continuum emission in the HST band is not significantly important, one could directly divide the two images product of the *HST*/ACS pipeline before any further reduction. If registration-image issues are not important, the same structures observed in the ‘processed images’ should still be visible. We perform this test for the particular cases of 3C 33 and 3C 234, two of the most spectacular objects in our sample. The morphologies and the shape of the scatter are similar to those observed after the full reduction process.

Overall, we conclude that the [O III]/H $\alpha$  variations and the scatter seen in Figures 2 and 6 respectively are generally reliable, and trace the spatial variations of the gas with different optical thickness and/or densities along the optical axis.

## REFERENCES

- Adhikari, T. P., Rózańska, A., Czerny, B., Hryniewicz, K., & Ferland, G. J. 2016, *ApJ*, 831, 68  
 Allen, M. G., Groves, B. A., Dopita, M. A., Sutherland, R. S., & Kewley, L. J. 2008, *ApJS*, 178, 20  
 Baldi, R. D., & Capetti, A. 2008, *A&A*, 489, 989  
 —. 2010, *A&A*, 519, A48+  
 Baldi, R. D., Capetti, A., Buttiglione, S., Chiaberge, M., & Celotti, A. 2013, *A&A*, 560, A81  
 Baldi, R. D., Capetti, A., & Giovannini, G. 2015, *A&A*, 576, A38  
 Baldi, R. D., Capetti, A., & Massaro, F. 2018, *A&A*, 609, A1  
 Baldi, R. D., et al. 2010, *ApJ*, 725, 2426  
 Balmaverde, B., Baldi, R. D., & Capetti, A. 2008, *A&A*, 486, 119  
 Balmaverde, B., & Capetti, A. 2006, *A&A*, 447, 97  
 Balmaverde, B., Capetti, A., & Grandi, P. 2006, *A&A*, 451, 35  
 Balmaverde, B., Capetti, A., Marconi, A., & Venturi, G. 2018, *A&A*, 612, A19



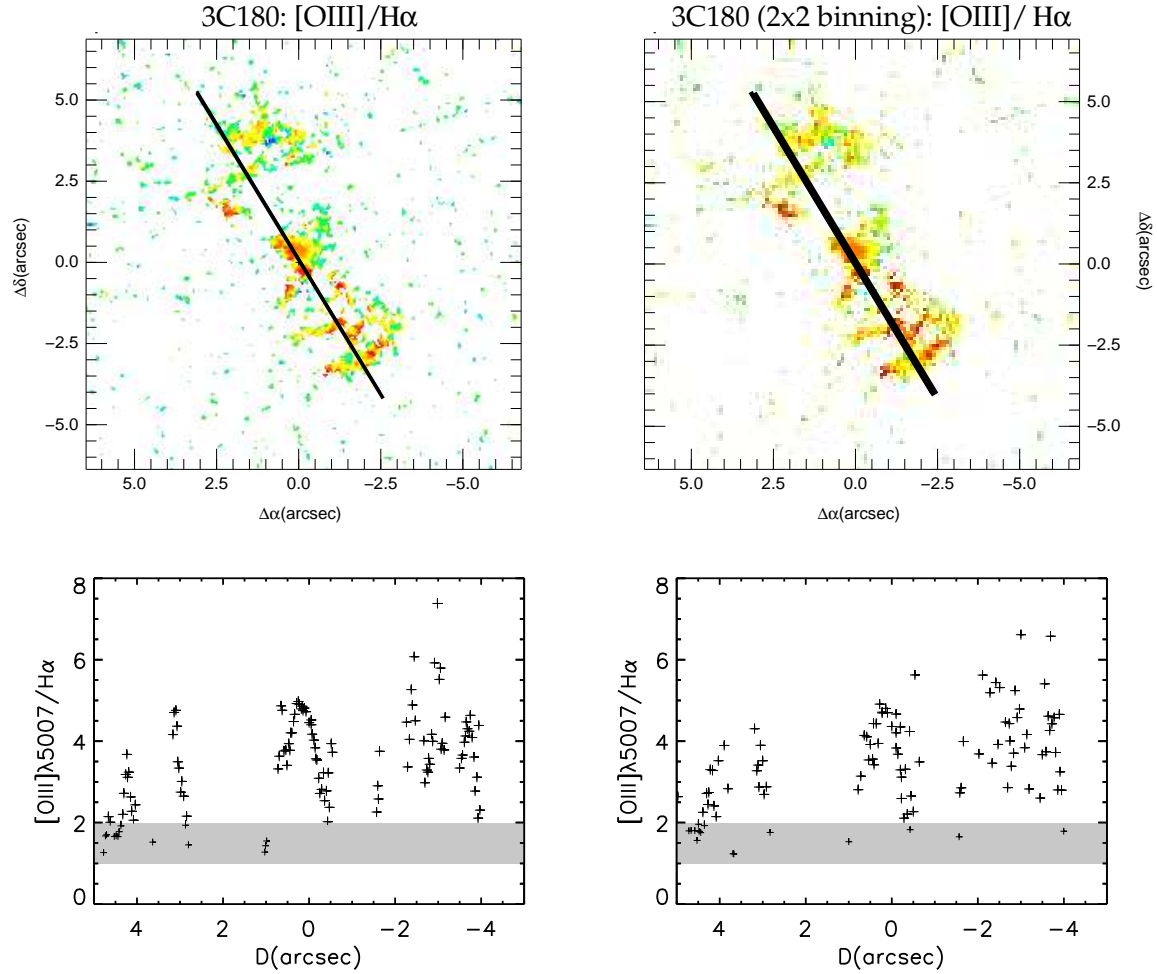


FIG. 12.— Top left: the spatial distribution of the  $[\text{O III}]/\text{H}\alpha$  line ratio for 3C 180. Top right: the spatial distribution of the  $[\text{O III}]/\text{H}\alpha$  line ratio obtained after binning the  $[\text{O III}]$  and the  $\text{H}\alpha + \text{N II}$  images using  $2 \times 2$  pixel binning mode. The black-solid lines drawn in the figures correspond to a section of the galaxy of 3 pixels of width, extended along the optical axis of the source. Bottom left: the  $[\text{O III}]/\text{H}\alpha$  line ratios plotted against the distance ( $D$ ) from the center of the galaxy. Bottom right: same as bottom left but for the top right figure. When generating these plots we used the section of the galaxy corresponding to the black, solid line in the top-left panel. In addition, we used the values in Column 6 and 7 in Table 3 to correct for  $[\text{O III}]\lambda 4959$  and  $[\text{N II}]\lambda\lambda 6949, 6983$  contribution to the flux in the band. As clear from the figure, the emission-line structures observed in the unbinned image are still visible after the binning.

Balmaverde, B., Capetti, A., Moiso, D., Baldi, R. D., & Marconi, A. 2016, *A&A*, 586, A48  
 Balmaverde, B., et al. 2012, *A&A*, 545, A143  
 Baum, S. A., & Heckman, T. 1989a, *ApJ*, 336, 681  
 —. 1989b, *ApJ*, 336, 702  
 Bennert, N., Falcke, H., Schulz, H., Wilson, A. S., & Wills, B. J. 2002, *ApJ*, 574, L105  
 Bennett, A. S. 1962a, *MNRAS*, 125, 75  
 —. 1962b, *MNRAS*, 68, 163  
 Best, P. N., & Heckman, T. M. 2012, *MNRAS*, 421, 1569  
 Best, P. N., Röttgering, H. J. A., & Longair, M. S. 2000, *MNRAS*, 311, 23  
 Binette, L., Courvoisier, T. J.-L., & Robinson, A. 1988, *A&A*, 190, 29  
 Binette, L., Magris, C. G., Stasińska, G., & Bruzual, A. G. 1994, *A&A*, 292, 13  
 Binette, L., Wilson, A. S., & Storchi-Bergmann, T. 1996, *A&A*, 312, 365  
 Birzan, L., Rafferty, D. A., Nulsen, P. E. J., McNamara, B. R., Röttgering, H. J. A., Wise, M. W., & Mittal, R. 2012, *MNRAS*, 427, 3468  
 Blandford, R. D., Netzer, H., Woltjer, L., Courvoisier, T. J.-L., & Mayor, M., eds. 1990, *Active Galactic Nuclei*  
 Boroson, T. A., & Green, R. F. 1992, *ApJS*, 80, 109  
 Bower, R. G., Benson, A. J., Malbon, R., Helly, J. C., Frenk, C. S., Baugh, C. M., Cole, S., & Lacey, C. G. 2006, *MNRAS*, 370, 645

Buttiglione, S., Capetti, A., Celotti, A., Axon, D. J., Chiaberge, M., Macchetto, F. D., & Sparks, W. B. 2009, *A&A*, 495, 1033  
 —. 2010, *A&A*, 509, A6+  
 —. 2011, *A&A*, 525, A28+  
 Capetti, A., Axon, D. J., Macchetto, F., Sparks, W. B., & Boksenberg, A. 1996, *ApJ*, 469, 554  
 Capetti, A., Robinson, A., Baldi, R. D., Buttiglione, S., Axon, D. J., Celotti, A., & Chiaberge, M. 2013, *A&A*, 551, A55  
 Capetti, A., Verdoes Kleijn, G., & Chiaberge, M. 2005, *A&A*, 439, 935  
 Capetti, A., et al. 2011, *A&A*, 527, L2+  
 Castignani, G., Chiaberge, M., Celotti, A., Norman, C., & De Zotti, G. 2014, *ApJ*, 792, 114  
 Chambers, K. C., Miley, G. K., & van Breugel, W. 1987, *Nature*, 329, 604  
 Chiaberge, M., Capetti, A., & Celotti, A. 1999, *A&A*, 349, 77  
 —. 2002a, *A&A*, 394, 791  
 Chiaberge, M., Gilli, R., Lotz, J. M., & Norman, C. 2015, *ApJ*, 806, 147  
 Chiaberge, M., Macchetto, F. D., Sparks, W. B., Capetti, A., Allen, M. G., & Martel, A. R. 2002b, *ApJ*, 571, 247  
 Chiaberge, M., & Marconi, A. 2011, *MNRAS*, 416, 917  
 Clark, N. E., Axon, D. J., Tadhunter, C. N., Robinson, A., & O'Brien, P. 1998, *ApJ*, 494, 546  
 Congiu, E., et al. 2017, *Frontiers in Astronomy and Space Sciences*, 4, 27



- Contini, M., Cracco, V., Ciroi, S., & La Mura, G. 2012, *A&A*, 545, A72
- Couto, G. S., Storchi-Bergmann, T., Axon, D. J., Robinson, A., Kharb, P., & Riffel, R. A. 2013, *MNRAS*, 435, 2982
- Couto, G. S., Storchi-Bergmann, T., & Schnorr-Müller, A. 2017, *MNRAS*, 469, 1573
- Cresci, G., & Maiolino, R. 2018, *Nature Astronomy*, 2, 179
- Cresci, G., et al. 2015, *A&A*, 582, A63
- Croton, D. J., et al. 2006, *MNRAS*, 365, 11
- Dasyra, K. M., Bostrom, A. C., Combes, F., & Vlahakis, N. 2015, *ApJ*, 815, 34
- de Koff, S., Baum, S. A., Sparks, W. B., Biretta, J., Golombek, D., Macchetto, F., McCarthy, P., & Miley, G. K. 1996, *ApJS*, 107, 621
- Dempsey, R., & Zakamska, N. L. 2018, *MNRAS*, 477, 4615
- Dicken, D., Tadhunter, C., Axon, D., Morganti, R., Inskip, K. J., Holt, J., González Delgado, R., & Groves, B. 2009, *ApJ*, 694, 268
- Dopita, M. A., & Sutherland, R. S. 1995, *ApJ*, 455, 468
- Erkens, U., Appenzeller, I., & Wagner, S. 1997, *A&A*, 323, 707
- Evans, I. N., & Dopita, M. A. 1985, *ApJS*, 58, 125
- Fabian, A. C. 1999, *MNRAS*, 308, L39
- , 2012, *ARA&A*, 50, 455
- Fabian, A. C., Sanders, J. S., Taylor, G. B., Allen, S. W., Crawford, C. S., Johnstone, R. M., & Iwasawa, K. 2006, *MNRAS*, 366, 417
- Fanaroff, B. L., & Riley, J. M. 1974, *MNRAS*, 167, 31P
- Fischer, T. C., et al. 2018, *ApJ*, 856, 102
- Floyd, D. J. E., et al. 2010, *ApJ*, 713, 66
- Fosbury, R. A. E., et al. 1982, *MNRAS*, 201, 991
- Freitas, I. C., et al. 2018, *MNRAS*, 476, 2760
- Gendre, M. A., Best, P. N., Wall, J. V., & Ker, L. M. 2013, *MNRAS*, 430, 3086
- Gómez-Guijarro, C., González-Martín, O., Ramos Almeida, C., Rodríguez-Espinosa, J. M., & Gallego, J. 2017, *MNRAS*, 469, 2720
- Groves, B. A., Dopita, M. A., & Sutherland, R. S. 2004, *ApJS*, 153, 75
- Gürkan, G., et al. 2015, *MNRAS*, 452, 3776
- Hainline, K. N., Hickox, R. C., Greene, J. E., Myers, A. D., Zakamska, N. L., Liu, G., & Liu, X. 2014, *ApJ*, 787, 65
- Hardcastle, M. J. 2004, *A&A*, 414, 927
- Hardcastle, M. J., Evans, D. A., & Croston, J. H. 2007, *MNRAS*, 376, 1849
- , 2009, *MNRAS*, 396, 1929
- Hardcastle, M. J., & Worrall, D. M. 2000, *MNRAS*, 314, 359
- Hardcastle, M. J., et al. 2013, *MNRAS*, 429, 2407
- Harrison, C. M., Costa, T., Tadhunter, C. N., Flütsch, A., Kakkad, D., Perna, M., & Vietri, G. 2018, *Nature Astronomy*, 2, 198
- Harrison, C. M., Thomson, A. P., Alexander, D. M., Bauer, F. E., Edge, A. C., Hogan, M. T., Mullaney, J. R., & Swinbank, A. M. 2015, *ApJ*, 800, 45
- Heckman, T. M., & Best, P. N. 2014, *ARA&A*, 52, 589
- Herbert, P. D., Jarvis, M. J., Willott, C. J., McLure, R. J., Mitchell, E., Rawlings, S., Hill, G. J., & Dunlop, J. S. 2010, *MNRAS*, 406, 1841
- Hill, G. J., & Lilly, S. J. 1991, *ApJ*, 367, 1
- Hine, R. G., & Longair, M. S. 1979, *MNRAS*, 188, 111
- Ho, L. C. 2008, *ARA&A*, 46, 475
- Holt, J., Tadhunter, C. N., & Morganti, R. 2003, *MNRAS*, 342, 227
- Hopkins, P. F., Robertson, B., Krause, E., Hernquist, L., & Cox, T. J. 2006, *ApJ*, 652, 107
- Howarth, I. 1983, *MNRAS*, 203, 301
- Ineson, J., Croston, J. H., Hardcastle, M. J., Kraft, R. P., Evans, D. A., & Jarvis, M. 2015, *MNRAS*, 453, 2682
- Ishibashi, W., Auger, M. W., Zhang, D., & Fabian, A. C. 2014, *MNRAS*, 443, 1339
- Jackson, N., & Rawlings, S. 1997, *MNRAS*, 286, 241
- Janssen, R. M. J., Röttgering, H. J. A., Best, P. N., & Brinchmann, J. 2012, *A&A*, 541, A62
- Kataoka, J., et al. 2011, *ApJ*, 740, 29
- Kewley, L. J., Groves, B., Kauffmann, G., & Heckman, T. 2006, *MNRAS*, 372, 961
- Kraemer, S. B., Schmitt, H. R., & Crenshaw, D. M. 2008, *ApJ*, 679, 1128
- Laing, R. A., Jenkins, C. R., Wall, J. V., & Unger, S. W. 1994, in *The First Stromlo Symposium: The Physics of Active Galaxies*. ASP Conference Series, Vol. 54, 1994, G.V. Bicknell, M.A. Dopita, and P.J. Quinn, Eds., p.201, 201+—
- Laor, A., Fiore, F., Elvis, M., Wilkes, B. J., & McDowell, J. C. 1997, *ApJ*, 477, 93
- Lavalley, M., Isobe, T., & Feigelson, E. 1992, in *Astronomical Society of the Pacific Conference Series*, Vol. 25, *Astronomical Data Analysis Software and Systems I*, ed. D. M. Worrall, C. Biemesderfer, & J. Barnes, 245+—
- Lea, S. M., & Holman, G. D. 1978, *ApJ*, 222, 29
- Livio, M. 1999, *Phys. Rep.*, 311, 225
- Lusso, E., et al. 2012, *MNRAS*, 425, 623
- Madrid, J. P., et al. 2006, *ApJS*, 164, 307
- Maiolino, R., Marconi, A., & Oliva, E. 2001, *A&A*, 365, 37
- Maiolino, R., & Rieke, G. H. 1995, *ApJ*, 454, 95
- Maksym, W. P., Fabbiano, G., Elvis, M., Karovska, M., Paggi, A., Raymond, J., Wang, J., & Storchi-Bergmann, T. 2016, *ApJ*, 829, 46
- Martel, A. R., et al. 1999, *ApJS*, 122, 81
- Massaro, F., et al. 2010, *ApJ*, 714, 589
- , 2012, *ApJS*, 203, 31
- McCarthy, P. J., van Breugel, W., Spinrad, H., & Djorgovski, S. 1987, *ApJ*, 321, L29
- McNamara, B. R., & Nulsen, P. E. J. 2012, *New Journal of Physics*, 14, 055023
- Morganti, R. 2017, *Frontiers in Astronomy and Space Sciences*, 4, 42
- Morganti, R., Robinson, A., Fosbury, R. A. E., di Serego Alighieri, S., Tadhunter, C. N., & Malin, D. F. 1991, *MNRAS*, 249, 91
- Morganti, R., Ulrich, M.-H., & Tadhunter, C. N. 1992, *MNRAS*, 254, 546
- Netzer, H., & Laor, A. 1993, *ApJ*, 404, L51
- Okamoto, T., Nemmen, R. S., & Bower, R. G. 2008, *MNRAS*, 385, 161
- Osterbrock, D. E. 1989, *Astrophysics of gaseous nebulae and active galactic nuclei* (Research supported by the University of California, John Simon Guggenheim Memorial Foundation, University of Minnesota, et al. Mill Valley, CA, University Science Books, 1989, 422 p.)
- Osterbrock, D. E., & Shuder, J. M. 1982, *ApJS*, 49, 149
- Owen, F. N. 1996, in *IAU Symposium*, Vol. 175, *Extragalactic Radio Sources*, ed. R. D. Ekers, C. Fanti, & L. Padrielli, 305+—
- Prescott, M., et al. 2018, *MNRAS*, 480, 707
- Prieto, M. A., Walsh, J. R., Fosbury, R. A. E., & di Serego Alighieri, S. 1993, *MNRAS*, 263, 10
- Privon, G. C., O’Dea, C. P., Baum, S. A., Axon, D. J., Kharb, P., Buchanan, C. L., Sparks, W., & Chiaberge, M. 2008, *ApJS*, 175, 423
- Ramos Almeida, C., Bessiere, P. S., Tadhunter, C. N., Inskip, K. J., Morganti, R., Dicken, D., González-Serrano, J. I., & Holt, J. 2013, *MNRAS*, 436, 997
- Ramos Almeida, C., Tadhunter, C. N., Inskip, K. J., Morganti, R., Holt, J., & Dicken, D. 2011, *MNRAS*, 410, 1550
- Ramos Almeida, C., et al. 2012, *MNRAS*, 419, 687
- Rampadarath, H., et al. 2018, *MNRAS*, 476, 2876
- Rawlings, S., & Saunders, R. 1991, *Nature*, 349, 138
- Rawlings, S., Saunders, R., Eales, S. A., & Mackay, C. D. 1989, *MNRAS*, 240, 701
- Revalski, M., Crenshaw, D. M., Kraemer, S. B., Fischer, T. C., Schmitt, H. R., & Machuca, C. 2018, *ApJ*, 856, 46
- Robinson, A., Binette, L., Fosbury, R. A. E., & Tadhunter, C. N. 1987, *MNRAS*, 227, 97
- Robinson, T., Tadhunter, C., Axon, D., & Robinson, A. 2000, *MNRAS*, 317, 922
- Roche, N., Humphrey, A., Lagos, P., Papaderos, P., Silva, M., Cardoso, L. S. M., & Gomes, J. M. 2016, *MNRAS*, 459, 4259
- Salomé, Q., Salomé, P., Combes, F., Hamer, S., & Heywood, I. 2016, *A&A*, 586, A45
- Santoro, F., Oonk, J. B. R., Morganti, R., Oosterloo, T. A., & Tremblay, G. 2015, *A&A*, 575, L4
- Sarzi, M., et al. 2010, *MNRAS*, 402, 2187
- Schlegel, J., Finkbeiner, D., & Davis, M. 1998, *ApJ*, 500, 525
- Seaton, M. 1979, *MNRAS*, 187, 73
- Shangguan, J., Ho, L. C., & Xie, Y. 2018, *ApJ*, 854, 158
- Shi, Y., et al. 2005, *ApJ*, 629, 88
- Silk, J., & Rees, M. J. 1998, *A&A*, 331, L1
- Smolčić, V. 2009, *ApJ*, 699, L43

- Smolčić, V., & Riechers, D. A. 2011, *ApJ*, 730
- Spinrad, H., Marr, J., Aguilar, L., & Djorgovski, S. 1985, *PASP*, 97, 932
- Stasińska, G., et al. 2008, *MNRAS*, 391, L29
- Storchi-Bergmann, T., Wilson, A. S., Mulchaey, J. S., & Binette, L. 1996, *A&A*, 312, 357
- Sun, A.-L., et al. 2018, *MNRAS*
- Tadhunter, C., Dicken, D., Morganti, R., Konyves, V., Ysard, N., Nesvadba, N., & Ramos Almeida, C. 2014, *MNRAS*, 445, L51
- Tadhunter, C., Dickson, R., Morganti, R., Robinson, T. G., Wills, K., Villar-Martin, M., & Hughes, M. 2002, *MNRAS*, 330, 977
- Tadhunter, C. N., Fosbury, R. A. E., Binette, L., Danziger, I. J., & Robinson, A. 1987, *Nature*, 325, 504
- Tadhunter, C. N., Metz, S., & Robinson, A. 1994, *MNRAS*, 268, 989
- Tadhunter, C. N., Morganti, R., Robinson, A., Dickson, R., Villar-Martin, M., & Fosbury, R. A. E. 1998, *MNRAS*, 298, 1035
- Tasse, C., Best, P. N., Röttgering, H., & Le Borgne, D. 2008, *A&A*, 490, 893
- Taylor, M. D., Tadhunter, C. N., & Robinson, T. G. 2003, *MNRAS*, 342, 995
- Tremblay, G. R., et al. 2009, *ApJS*, 183, 278
- Vasudevan, R. V., Fabian, A. C., Gandhi, P., Winter, L. M., & Mushotzky, R. F. 2010, *MNRAS*, 402, 1081
- Villar Martín, M., Bellocchi, E., Stern, J., Ramos Almeida, C., Tadhunter, C., & González Delgado, R. 2015, *MNRAS*, 454, 439
- Wagner, A. Y., Bicknell, G. V., & Umemura, M. 2012, *ApJ*, 757, 136
- Westhues, C., et al. 2016, *AJ*, 151, 120
- Whittam, I. H., Prescott, M., McAlpine, K., Jarvis, M. J., & Heywood, I. 2018, *MNRAS*, 480, 358
- Williams, D. R. A., et al. 2017, *MNRAS*, 472, 3842
- Wills, B. J., Netzer, H., Brotherton, M. S., Han, M., Wills, D., Baldwin, J. A., Ferland, G. J., & Browne, I. W. A. 1993, *ApJ*, 410, 534
- Zheng, W., Kriss, G. A., Telfer, R. C., Grimes, J. P., & Davidsen, A. F. 1997, *ApJ*, 475, 469
- Zirbel, E. L. 1996, *ApJ*, 473, 713
- . 1997, *ApJ*, 476, 489
- Zirbel, E. L., & Baum, S. A. 1995, *ApJ*, 448, 521